

THE CENTRAL REGION OF BARRED GALAXIES: MOLECULAR ENVIRONMENT,  
STARBURSTS, AND SECULAR EVOLUTION

SHARDHA JOGEE<sup>1</sup>, NICK SCOVILLE<sup>2</sup>, & JEFFREY D. P. KENNEY<sup>3</sup>  
sj@astro.as.utexas.edu, nzs@astro.caltech.edu, kenney@astro.yale.edu

*Accepted by The Astrophysical Journal*

ABSTRACT

Stellar bars drive gas into the circumnuclear (CN) region of galaxies. To investigate the fate of the CN gas and star formation (SF), we study a sample of barred non-starbursts and starbursts with high-resolution CO, optical, H $\alpha$ , RC, Br $\gamma$ , and *HST* data, and find the following. (1) The inner kpc of bars differs markedly from the outer disk. It hosts molecular gas surface densities  $\Sigma_{\text{gas-m}}$  of 500–3500  $M_{\odot} \text{pc}^{-2}$ , gas mass fractions of 10 to 30%, and epicyclic frequencies of several 100–1000  $\text{km s}^{-1} \text{kpc}^{-1}$ . Consequently, in the CN region, gravitational instabilities can only grow at high gas densities and on short timescales, explaining in part why powerful starbursts reside there. (2) Across the sample, we find bar pattern speeds with upper limits of 43 to 115  $\text{km s}^{-1} \text{pc}^{-1}$  and outer inner Lindblad resonance (OILR) radii of  $> 500 \text{pc}$ . (3) Barred starbursts and non-starbursts have CN SFRs of 3–11 and 0.1–2  $M_{\odot} \text{yr}^{-1}$ , despite similar CN gas mass.  $\Sigma_{\text{gas-m}}$  in the starbursts is larger (1000–3500  $M_{\odot} \text{pc}^{-2}$ ) and close to the Toomre critical density over a large region. (4) Molecular gas makes up 10%–30% of the CN dynamical mass, and fuels large CN SFRs in the starbursts, building young, massive, high  $V/\sigma$  components. Implications for secular evolution along the Hubble sequence are discussed.

*Subject headings:* galaxies: starburst—galaxies: ISM—galaxies: structure—galaxies: kinematics and dynamics—galaxies: evolution

1. INTRODUCTION

It is widely recognized that non-axisymmetries, such as large-scale stellar bars, facilitate the radial transfer of angular momentum in disk galaxies, thus driving their dynamical and secular evolution (e.g., Pfenniger & Norman 1990; Friedli & Benz 1995; Athanassoula 1992; Kormendy 1993; Kormendy & Kennicutt 2004; review by Jogee 2004 and references therein). Numerous studies (e.g., Knapen et al. 2000; Eskridge et al. 2000) have shown that the majority ( $> 70\%$ ) of nearby disk galaxies host large-scale stellar bars. Using *HST* Advanced Camera for Surveys (ACS) data, Jogee et al. (2004a,b) find that strong bars remain frequent from the present day out to lookback times of 8 Gyr ( $z \sim 1$ ), and infer that bars are long-lived features with a lifetime well above 2 Gyr. A non-declining optical bar fraction out to  $z \sim 1$  is also confirmed by Elmegreen et al. (2004). These findings suggest that bars can influence a galaxy over a significant part of its lifetime. Compelling evidence that bars efficiently drive gas from the outer disk into the inner kpc comes from the larger central molecular gas concentrations observed in barred galaxies compared to unbarred galaxies (Sakamoto et al. 1999).

However, few high resolution studies based on large samples exist of the fate of gas once it reaches the inner kpc of a bar. In this study, we use high resolution ( $2''$ ;  $\sim 200 \text{pc}$ ) CO ( $J=1-0$ ) observations, optical, NIR, H $\alpha$ , radio continuum (RC), Br $\gamma$ , and archival *HST* data in order to characterize the molecular environment, the onset of starbursts, and the dynamical evolution in the circumnuclear region of barred galaxies. Our sample consists of ten carefully selected nearby barred non-starbursts and starbursts,

including some of the most luminous starbursts within 40 Mpc. Given the time-consuming nature of interferometric  $2''$  CO observations, this is one of the largest sample studied at this resolution. CO observations of nearby galaxies have in the past often been limited to a few individual systems, and it is only in recent years that we have seen a systematic mapping of sizable samples (10–12) of nearby galaxies (e.g., Baker 2000; Jogee 1999). Complementary surveys such as the  $7''$  resolution BIMA CO(1–0) Survey of Nearby Galaxies (SONG; Regan et al. 2001; Helfer et al. 2001) or the NMA–OVRO  $4''$  resolution CO(1–0) survey of galaxies (Sakamoto et al. 1999) are better suited for studying extended structures or the average properties within the inner kpc.

The main sections of the paper are as follows. § 2 outlines the sample selection and § 3 the properties of stellar bars in the sample galaxies. The imaging and interferometric CO observations are covered in § 4. § 6 highlights the extreme molecular environment which has built up in the inner kpc of barred galaxies and discusses its implication. In § 7, we estimate the SFR in the circumnuclear region using different tracers such as Br $\gamma$ , RC, and FIR luminosities. In § 8, we compare the circumnuclear molecular gas in the barred starbursts and non-starbursts in order to investigate why they have such different SFR/ $M_{\text{H}_2}$  in the inner few kpc. In § 9, we push these investigations further by comparing the observed circumnuclear gas surface density to the critical density for the onset of gravitational instabilities. In § 10, we investigate where the molecular gas has piled up with respect to the dynamical resonances of the bar. In § 11, we discuss the results within the context of bar-driven secular evolutionary scenarios. For readers

<sup>1</sup> Department of Astronomy, University of Texas at Austin, 1 University Station C1400, Austin, TX 78712-0259

<sup>2</sup> Division of Physics, Mathematics, and Astronomy, MS 105-24, California Institute of Technology, Pasadena, CA 91125

<sup>3</sup> Yale University Astronomy Department, New Haven, CT 06520-8101

interested in specific galaxies, § 12 describes the molecular gas distribution and kinematics of individual galaxies. § 13 summarizes our main results.

## 2. SAMPLE SELECTION

In this study, we wish to investigate the properties of molecular gas in the circumnuclear region (inner 1–2 kpc) of barred galaxies, the parameters which control when they form stars, and the reasons for the large range in  $\text{SFR}/M_{\text{H}_2}$  seen in the inner few kpc. In order to effectively address these questions, we will carry out high resolution ( $2''$ ) interferometric CO observations (§ 2) of the sample galaxies. However, when selecting the sample prior to such observations, we necessarily have to use existing low resolution ( $45''$ ) single dish CO luminosities (e.g., Young et al. 1995) as a first measure of the mass of cold molecular hydrogen (Dickman, Snell, & Schloerb 1986; Scoville & Sanders 1987). We obtain a measure of the massive SF rate within the same  $45''$  aperture from the RC luminosity ( $L_{\text{RC}}$ ) at 1.5 GHz (e.g., Condon et al. 1990). Empirical evidence such as the FIR-RC correlation (Condon et al. 1982) the  $\text{H}\alpha$ -RC correlation (Kennicutt 1983), as well as simple physical models (e.g., Condon 1992) suggest that the RC luminosity at 1.5 GHz is a good tracer of the massive SFR on sufficiently large scales. The FIR-radio correlation also appears to hold locally within individual galaxies at least on scales  $\geq 1$  kpc (Condon 1992).

We selected ten sample galaxies which satisfy the following criteria: (i) We avoided systems with very low CO luminosities, which require inordinate investments of time for interferometric CO observations. Instead, we picked galaxies which are fairly gas-rich but still span an order of magnitude in circumnuclear molecular gas content (a few  $\times 10^8$ – $10^9 M_{\odot}$ ) and a wide range in SFR per unit mass of gas. These galaxies were chosen from different parts of the  $L_{\text{RC}}/L_{\text{CO}}$  versus  $L_{\text{CO}}$  plane (Fig. 1); (ii) They have moderate distances ( $D=10$  to 34 Mpc) so that the  $2''$  interferometric CO observations (§ 2) can accurately resolve the gas distribution and kinematics on scales of 100–300 pc; (iii) They have inclinations below 70 deg so that we can minimize extinction problems and get a good handle on the gas kinematics; (iv) They have complementary high resolution observations such as Brackett- $\gamma$  fluxes (Puxley, Hawarden, & Mountain 1988, 1990), and/or 5 GHz RC observations (Saikia et al. 1994) for tracing the SF activity at resolutions comparable to that of the  $2''$  interferometric CO observations; (v) We excluded major mergers with strong morphological distortions in the inner kpc region as the associated highly non-axisymmetric gas distributions and large non-circular motions often preclude an accurate dynamical analysis. This is discussed further in § 3.

Table 1 gives the general properties of the sample. Table 2 shows  $L_{\text{CO}}$ ,  $L_{\text{RC}}$ , and the luminosities of different SF tracers within various apertures. Fig. 1 shows the sample galaxies plotted in the  $L_{\text{RC}}/L_{\text{CO}}$  versus  $L_{\text{CO}}$  plane. The term ‘starburst’ is used in a multitude of ways in the literature: in some cases, a large SF luminosity alone is used to identify a star-forming region as a starburst, while in other cases the duration of the burst is also taken into account. In this work, the term circumnuclear starburst refers to a luminous and short-lived episode of SF in the inner kpc region. We adopt a working definition where the circumnu-

clear starbursts have a ratio ( $L_{\text{RC}}/L_{\text{CO}}$ ) above 0.5, which corresponds to a gas consumption timescale ( $M_{\text{H}_2}/\text{SFR}$ ) below 1 Gyr, under standard assumptions. The Milky Way has a ( $\text{SFR}/M_{\text{H}_2}$ ) ratio above  $10^{-9} \text{ yr}^{-1}$ , and would be a non-starburst. The circumnuclear starbursts in our sample (NGC 470, NGC 2782, NGC 3504, NGC 4102, and NGC 4536) are marked on Fig. 1 and are among the most luminous starbursts within 40 Mpc. While they are selected on the basis of RC luminosities, the circumnuclear starbursts also have a large FIR luminosity, comparable to that of the prototypical starburst M82, which is marked for reference on Fig. 1. Four of the starbursts (NGC 470, NGC 2782, NGC 3504, and NGC 4102) in fact belong to Devereux’s (1989) sample of the twenty brightest nearby ( $15 < D < 40$  Mpc) circumnuclear starbursts selected on the basis of a high far-infrared luminosity ( $L_{\text{FIR}} > 2.9 \times 10^9 L_{\odot}$ ) and central 10  $\mu\text{m}$  luminosity ( $L_{10\mu\text{m}} > 6 \times 10^8 L_{\odot}$ ).

Note that in Figure 1, *the SFR per unit mass of molecular gas in the central 45'' spans more than an order of magnitude for a given total mass of molecular gas*. Can this range be due to the different distance of the sample galaxies causing the  $45''$  beam to encompass regions of different sizes? We believe this is unlikely because most of the SF activity is concentrated well inside the  $45''$  beam, and 80% of the galaxies have comparable distances in the range 10–20 Mpc. In fact, a similar range in the SFR per unit mass of molecular gas is obtained if the central 10 micron luminosity (Giuricin et al. 1994; Devereux 1989) is used instead of the radio continuum to trace the SFR. It is also valid to ask whether variations in the CO-to- $\text{H}_2$  conversion factor  $\chi$  between the galaxies might reduce the range in ( $\text{SFR}/M_{\text{H}_2}$ ) on Fig. 1. We refer the reader to § 5 for a discussion on  $\chi$ , but note here that the somewhat lower conversion factor in starbursts suggested by some studies (Aalto et al. 1994, 1995), would in fact *increase* rather than reduce the range in ( $\text{SFR}/M_{\text{H}_2}$ ) in Fig. 1. Therefore, it appears that the range in  $\text{SFR}/M_{\text{H}_2}$  within the sample is a truly inherent property.

## 3. STELLAR BARS AND TIDAL INTERACTIONS IN THE SAMPLE

It is widely held that large-scale stellar bars, whether tidally or spontaneously induced, efficiently drive gas from the outer disk into the inner kpc via gravitational torques, thereby building large gas concentrations (§ 1). In fact, bars are found to be the main driver of gas inflows into the circumnuclear region even in interacting systems, namely, in a large fraction of minor mergers, most intermediate 1:3 mass ratio mergers and the early phases of most major mergers (Jogee 2004 and references therein). The properties of the sample galaxies, which have moderate to large amounts of circumnuclear molecular gas in the range of a few  $\times (10^8$ – $10^9) M_{\odot}$ , are consistent with this picture. While we have excluded systems with strong morphological distortions (§ 2), all of the sample galaxies, except for NGC 6951, show some evidence for tidal interaction in the recent past, or are in environments where they could potentially have interacted with or accreted other galaxies. All of them host large-scale stellar bars and oval distortions, which in some cases appear to be tidally triggered.

Table 3 illustrates the evidence for recent tidal interactions. NGC 470 is interacting with the large S0 galaxy

NGC 474. NGC 2782 appears to have undergone a close, recent interaction with another smaller disk galaxy, and its properties have been modeled with an intermediate mass ratio (1:4) interaction by Smith (1994). NGC 3359 has a nearby companion. NGC 3504, NGC 4314, and NGC 4102 dwell in groups, while NGC 4569 and NGC 4536 are part of the Virgo cluster. As described below, NGC 4569 shows several indications of a recent tidal disturbance.

There is evidence for stellar bars and oval distortions in all the sample galaxies, according to our optical  $R$ -band and NIR images, as well as the Third Reference Catalog of Bright Galaxies (RC3; de Vaucouleurs et al. 1991; Table 3). Figs. 2a-c illustrate the prominent bars in NGC 3504, NGC 4314, and NGC 6951. In other cases such as NGC 4102, NGC 4536, or NGC 2782, there is less conspicuous evidence for a large-scale bar. Both the  $K$  (Fig. 2d) and  $R$ -band images of NGC 4102 reveal a weak oval distortion, with a surface brightness profile reminiscent of a lens (Jogee & Kenney 1996). This may be the remnant of a weakened or destroyed bar. In NGC 4536, despite the large inclination (66 deg), prominent spiral arms in the outer disk, appear to branch out from an oval structure, suggesting the presence of a large-scale stellar bar. Isophotal analysis of NIR images also indicate the presence of nested nuclear stellar bars in NGC 2782 (Jogee, Kenney, & Smith 1999; § 12) and NGC 4314 (Friedli et al. 1996; § 12).

In the non-starburst NGC 3359 and NGC 4569, the stellar bar may have been recently tidally triggered. After comparing simulation results (Friedli, Benz, & Kennicutt 1994) with the observed properties of NGC 3359, such as the presence of HII regions along the bar and the abundance gradient profile, Martin & Roy (1995) claim that the bar in NGC 3359, is younger than a Gyr. A nearby companion (Ball 1986) may have tidally triggered this bar. In NGC 4569, the K-band isophotes (§ 8.1) in the inner 45'' (3.6 kpc) are significantly more elongated than those of the outer disk, and suggest the presence of a stellar bar-like feature that lies at a P.A. of  $\sim 15$  deg and extends outside the boxy bulge of diameter 30'' (2.9 kpc). The bar is more elongated to the north than to the south and the bulge isophotes also show east-west asymmetries. Furthermore, optical images (e.g., Sandage & Bedke 1994) show a warp in the outer stellar disk. A merger event or tidal interaction is likely to be responsible for the asymmetries in the stellar and CO (§ 8.1) morphologies. Ram pressure stripping which was previously invoked to account for the HI properties (Kenney & Young 1989; Cayatte et al. 1994) primarily affects the diffuse atomic gas only.

## 4. OBSERVATIONS

### 4.1. CO ( $J=1 \rightarrow 0$ ) observations

Table 4 describes the CO observations and channel maps. For most of the sample galaxies (NGC 470, NGC 2782, NGC 3310, NGC 4102, NGC 4536, NGC 4569, and NGC 3359), 2'' observations of the CO ( $J=1 \rightarrow 0$ ) line whose rest frequency is 115.27 GHz were made between 1995 and 2002 with the OVRO millimeter-wave interferometer (Padin et al. 1991). The other four were observed previously by Kenney et al. (1992; NGC 3351 and NGC 6951; 1993; NGC 3504) and Benedict et al. (1996; NGC 4314). As of 1996, the array consists of six 10.4-m anten-

nae with a primary HPBW of 65'' at 115 GHz. The seven galaxies were observed in the low, equatorial, and high resolution configurations with projected baselines ranging from 15 to 242 m. Data were obtained simultaneously with an analog continuum correlator of bandwidth 1 GHz and a digital spectrometer set-up which produced four independent modules that each have 32 channels with a velocity resolution of 10.4 km s<sup>-1</sup>. For our observations, the modules were partially overlapping and covered a total bandwidth of 1200 km s<sup>-1</sup> with 116 frequency channels. We corrected for temporal phase variations by interspersing integrations on the galaxy with observations of a phase calibrator (typically a quasar) every 20-25 minutes. Passbands were calibrated on the bright quasars 3C273, 3C84, and 3C345. The absolute flux scale, determined from observations of Uranus, Neptune, and 3C273, is accurate to 20%. The passband and flux calibration of the data were carried out using the Owens Valley millimeter array software (Scoville et al. 1993). We used the NRAO AIPS software to Fourier transform the calibrated uv data and deconvolve the channel maps with the 'CLEAN' algorithm as implemented in the AIPS tasks 'MX' and 'IMAGR'. Channel maps with both uniform and natural weighting were made for the galaxies. The naturally weighted maps capture more of the low signal-to-noise emission, but have lower spatial resolution.

### 4.2. Optical observations

We observed the ten sample galaxies using the Wisconsin Indiana Yale NOAO (WIYN) 3.5-m telescope at Kitt Peak National Observatory (KPNO), and the 0.9-m telescope at KPNO. On the WIYN telescope we used a 2048 x 2048 S2KB CCD with a plate scale of 0.2''/pixel, and a field of view of 6.8' x 6.8'. On the 0.9-m, the 2048 x 2048 T2KA CCD had a plate scale of 0.68''/pix, and field of view of 23.2' x 23.2'. The galaxies were imaged with broad-band Harris  $BVRI$  filters, narrow-band filters centered on the appropriately redshifted  $H\alpha + [N II]$  6563 6583 Å emission lines, and narrow off-line filters centered on a wavelength  $\sim 80$  Å redward of the  $H\alpha + [NII]$  line. The latter images are used to subtract stellar continuum from the  $H\alpha + [NII]$  image, and the continuum bandpass in this region is sufficiently close to the  $H\alpha + [NII]$  emission line that spectral color correction terms are generally negligible (Taylor et al. 1994). Standard fields of Landolt stars (e.g., PG0918+029, PG1047+003, PG1323-086, WOLF 629, SA110-502) were observed throughout the night over a range of airmasses for extinction correction. For some galaxies, where we had photometric conditions, exposures of the galaxy and of spectrophotometric standards at similar airmasses were taken for flux calibrating the  $H\alpha + [NII]$  observations. The IRAF Package was used for data reduction. After bias-subtraction and flat-fielding, the images in each filter were registered using unsaturated field stars, combined, and cleaned free of cosmic rays. After sky subtraction, the off-line narrow-band image was subtracted from the on-line image to obtain continuum-free  $H\alpha + [NII]$  line images. Where available, observations of spectrophotometric standards were used to flux calibrate the line.

## 5. CIRCUMNUCLEAR MOLECULAR GAS CONTENT

The mass of molecular hydrogen ( $M_{\text{H}_2}$ ) is estimated from the total flux using the relation (e.g., Scoville et al. 1987; Kenney & Young 1989)

$$\frac{M_{\text{H}_2}}{M_{\odot}} = 1.1 \times 10^4 \left( \frac{\chi}{2.8 \times 10^{20}} \right) (D^2) \left( \int S_{\text{CO}} dV \right) \quad (1)$$

where  $D$  is the distance in Mpc,  $\int S_{\text{CO}} dV$  is the integrated CO line flux in  $\text{Jy km s}^{-1}$ ,  $\chi$  is the CO-to- $\text{H}_2$  conversion factor, defined as the ratio of the beam-averaged column density of hydrogen to the integrated CO brightness temperature ( $N(\text{H}_2)/I_{\text{CO}}$ ).

The CO-to- $\text{H}_2$  conversion factor  $\chi$  depends on many factors including the metallicity of the gas, the dust column density, the ambient radiation field, the physical conditions in the gas, and the optical thickness of the line. All the sample targets are massive spirals and are likely to have solar or super-solar metallicities (Vila-Costas & Edmunds 1992). In this regime, the CO line is optically thick and there is only a weak dependence of  $\chi$  on metallicity (e.g., Elmegreen 1989) so that our use of a single  $\chi$  value across the sample is justified.

Values of  $\chi$  for molecular clouds in the Milky Way range from 1.8 to  $4.5 \times 10^{20} (\text{K km s}^{-1})^{-1}$ , based on different methods such as comparisons of the integrated  $^{13}\text{CO}$  intensities with the visual extinction (e.g., Dickman 1975), observations of  $\gamma$  ray fluxes (e.g., Bloemen et al. 1986; Strong et al. 1988), and virial equilibrium considerations (e.g., Dickman et al. 1986; Scoville et al. 1987; Solomon et al. 1987). It is arguable whether a Milky Way conversion factor applies to the actively star-forming circumnuclear regions of galaxies, where the temperatures and densities are much higher. For clouds in virial equilibrium,  $\chi$  depends on  $\rho^{0.5}/T_{\text{B}}$  (e.g., Scoville & Sanders 1987), where  $T_{\text{B}}$  is the CO brightness temperature averaged over the cloud and  $\rho$  is the density. One might argue, therefore, that the effects of elevated temperatures and densities will partially offset each other. On the other hand, the gas may not be in virial equilibrium and multiple-line studies combined with radiative transfer modeling (e.g., Wall & Jaffe 1990; Helfer & Blitz 1993; Aalto et al. 1994, 1995) have suggested that  $\chi$  is lower by a factor of  $\sim 3$  in the centers of some starburst galaxies, as compared to the Milky Way. However, given the absence of multiple-line studies or determinations of  $\chi$  in our sample galaxies, we adopted in this paper the value of  $2.8 \times 10^{20} (\text{K km s}^{-1})^{-1}$  that was derived for the inner Galaxy (Bloemen et al. 1986), while bearing in mind the possible uncertainties.

Table 5 shows the CO flux and the mass of molecular hydrogen detected by the interferometric observations. In most galaxies, we capture a large fraction (60 to 90 %) of the CO flux detected by single dish observations. We find massive gas concentrations –  $3 \times 10^8$  to  $2 \times 10^9 M_{\odot}$  of molecular hydrogen – in the inner 2 kpc radius of the sample galaxies. In particular, many galaxies with different RC luminosities within the central  $45''$  (e.g., NGC 6951 and NGC 4569 as compared to NGC 2782, NGC 3504, and NGC 4102) can have quite comparable circumnuclear molecular hydrogen content ( $\sim 1 - 2 \times 10^9 M_{\odot}$ ).

Fig. 3 shows the CO total intensity (moment 0) maps, the size of the synthesized beam and the position of the large-scale stellar bar for the sample galaxies. There is a wide variety of CO morphologies ranging from relatively

axisymmetric annuli or disks (NGC 4102, NGC 3504, NGC 4536, NGC 470, and NGC 4314) to elongated double-peaked and spiral morphologies (starburst NGC 2782 and non-starbursts NGC 3351 and NGC 6951). We refer the reader to § 8 for a comparison of the molecular gas properties in the starbursts and non-starbursts, and to § 12 for a description of the individual galaxies.

## 6. THE EXTREME MOLECULAR ENVIRONMENT IN THE INNER KPC OF BARRED SPIRALS AND ITS IMPLICATIONS

+

Table 6 illustrates how the molecular environment that has developed in the circumnuclear region of the barred spirals differs markedly from that present in the outer disk of galaxies. The implications for the inner kpc are outlined below.

**(i) Gas densities and mass fraction:** We compute the molecular gas surface densities ( $\Sigma_{\text{gas-m}}$ ) by deprojecting the moment 0 map and computing the azimuthally averaged surface density of molecular hydrogen ( $\Sigma_{\text{H}_2}$ ) as a function of radius in the galactic plane, assuming a standard CO-to- $\text{H}_2$  conversion factor. We add in the contribution of He using  $\Sigma_{\text{gas-m}} = A_Z \times \Sigma_{\text{H}_2}$ , where  $A_Z = 1.36$  for an assumed solar metallicity ( $Z = 0.02$ ,  $X=0.72$ ,  $Y=0.26$ ). The peak gas surface density  $\Sigma_{\text{gas-m}}$  in the inner kpc of these galaxies ranges from  $500\text{-}3500 M_{\odot} \text{ pc}^{-2}$ .

To estimate what fraction of the dynamical mass is in molecular form, we first calculate the total dynamical mass ( $M_{\text{dyn}}$ ) interior to radius  $R$  from the circular speed  $V_c$ :

$$M_{\text{dyn}}(R) = \frac{V_c^2(R) R \beta}{G} \quad (2)$$

where  $G$  is the gravitational constant and  $\beta$  depends on the shape of the mass distribution.  $\beta=1$  for a spherically symmetric mass distribution and is slightly lower for flattened configurations. For an exponential disk, we can overestimate the true dynamical mass by at most 1.3 if we assume  $\beta=1$  (Binney & Tremaine 1987). We estimate  $V_c$  and the CO rotation curve in the central 1-2 kpc radius from the CO position-velocity (p-v) plots. We can more effectively identify different kinematic components (e.g., circular motions, azimuthal streaming motions, radial inflow motions, and vertical outflow motions) in gas of different intensities from p-v plots along the kinematic major and minor axes than from moment 1 maps, which reflect only the intensity-weighted average values. In particular, we estimate  $V_c$  by taking the CO velocity at which the intensity levels peak at each radius along the kinematic major axis. The values of  $V_c$  estimated in this manner show good agreement with the rotation curve derived from  $\text{H}\alpha$  emission spectra (Jogee 1999) in cases where both data are available (e.g., NGC 4102, NGC 4536, NGC 3351, NGC 4569, NGC 6951). In regions where the gas shows evidence of non-circular motions in the p-v plots, estimates of  $V_c$  will be somewhat uncertain. We therefore derive  $V_c$  only for galaxies where the kinematics are relatively ordered and dominated by circular motions (§ 8).

In summary, we find that the inner kpc of the 10 barred spirals in our sample hosts peak molecular gas surface densities of  $500\text{-}3500 M_{\odot} \text{ pc}^{-2}$  and molecular gas mass fractions of 10 to 30 %. *These densities are at least an order*

of magnitude higher than the typical average atomic and molecular gas surface densities ( $1-100 M_{\odot} \text{ pc}^{-2}$ ) in the outer disk of normal spirals (Deharveng et al. 1994; Kennicutt 1998), or the gas surface density ( $200 M_{\odot} \text{ pc}^{-2}$ ) of a typical giant molecular cloud in the outer disk of the Milky Way (Scoville & Sanders 1987). Such large molecular gas surface densities and mass fraction in the inner kpc can *enhance the self gravity and clumpiness of the gas and produce stronger gravitational coupling between the gas and the stars* (e.g., Shlosman et al. 1989; Jog & Solomon 1984). The resulting two-fluid disk will be more unstable to gravitational instabilities than a purely stellar one-fluid disk (Jog & Solomon 1984; Elmegreen 1995).

Furthermore, as the gas becomes more clumpy dynamical friction might become an increasingly important transport mechanism at low radii. For instance, in the case of a gas clump which has a mass  $M$  and a speed  $v$  at radius  $r$ , the timescale  $t_{df}$  on which dynamical friction operates is  $\propto (r^2 v/M \ln\Lambda)$ , where  $\ln\Lambda$  is the Coulomb logarithm (Binney & Tremaine 1987). For  $M=10^8 M_{\odot}$ ,  $v \sim 300 \text{ km s}^{-1}$ ,  $r=200 \text{ pc}$ ,  $t_{df}$  is as short as  $\sim 3 \times 10^6$  years.

**(ii) Onset and growth of gravitational instabilities:** For a thin differentially rotating gas disk, support against gravitational instabilities is provided by pressure forces on small scales, and by Coriolis forces from rotation on large scales. The Coriolis forces depend on the epicyclic frequency of oscillations  $\kappa$  which is a function of the circular speed  $V_c$ :

$$\kappa = \sqrt{\frac{2V_c}{R} \left( \frac{V_c}{R} + \frac{dV_c}{dR} \right)}. \quad (3)$$

We estimate  $\kappa$  from the CO and H $\alpha$  rotation curves, bearing in mind that uncertainties exist in regions where there are non-circular motions. However, even uncertainties of a factor of a few do not change the basic expectations of very high epicyclic frequencies  $\kappa$  of a few 100 to several  $1000 \text{ km s}^{-1} \text{ kpc}^{-1}$ ) in the inner 500 pc. These very high epicyclic frequencies coupled with the moderately large gas velocity dispersions ( $10-40 \text{ km s}^{-1}$ ) *cause the critical density ( $\Sigma_{\text{crit}}$ ) for the onset of gravitational instabilities to shoot up to several  $100-1000 M_{\odot} \text{ pc}^{-2}$* . Although hard to trigger, once triggered, these instabilities have a short growth timescale ( $t_{\text{GI}}$ ) of a few Myrs for the most unstable wavelength:

$$t_{\text{GI}} = \frac{\sigma}{\pi G \Sigma_{\text{gas}}} \quad (4)$$

In other words, *the molecular environment and dynamical parameters of the inner kpc naturally force gravitational instabilities to set in and to grow in a “burst” mode defined by high density and short timescales*. This may explain, at least in part, why the most intense starbursts tend to be found in the inner kpc of galaxies.

It is also important to note that the growth timescale ( $t_{\text{GI}}$ ) of a few Myr in the inner kpc is comparable to the lifetime of an OB star. As a result, the fraction of molecular gas mass converted into stars before cloud complexes are disrupted by massive stars can be higher in the circumnuclear region than in the outer disk. The high pressure, high turbulence ISM may also favor more massive clusters as suggested by some authors (e.g., Elmegreen et al.

1993). It is relevant that 80 % of the sample galaxies show super star clusters.

**(iii) ULIRGs as scaled-up local starbursts?** In the circumnuclear region of the ULIRG Arp 220 (Scoville, Yun, & Bryant 1997), the conditions observed seem to be even more extreme than those in the inner kpc of the local barred starbursts: a gas surface density  $\sim 10^4 M_{\odot} \text{ pc}^{-2}$ , a velocity dispersion  $\sigma \sim 90 \text{ km s}^{-1}$ , and an epicyclic frequency  $\kappa \sim$  several  $1000 \text{ km s}^{-1} \text{ kpc}^{-1}$  (Table 6). Observations of these quantities at comparable resolution do not exist for other ULIRGs, but if Arp 220 is a proto-typical ULIRG, then Table 6 suggests that *the circumnuclear molecular environment of ULIRGs is a scaled-up version of that developed by the local weakly-interacting starbursts in our sample*. This scaled-up molecular environment may be the result of the the stronger external triggers acting on ULIRGs, which are generally strongly interacting systems, often involving mergers of comparably massive spirals. Such interactions can pile gas to very high densities in the inner kpc and produce larger turbulent linewidths, thereby boosting the critical density  $\Sigma_{\text{crit}}$  at which gravitational instabilities set in and ensuring the conditions for a super-starburst.

## 7. THE CIRCUMNUCLEAR STAR FORMATION RATE

When using the  $45''$  single dish CO map as a measure of the circumnuclear gas content (e.g., in § 2), it was appropriate to use the RC luminosity within a similar  $45''$  aperture as a measure of the circumnuclear SFR. The  $45''$  aperture corresponds to an aperture with a 2 kpc radius at the mean sample distance of 20 Mpc. However, now that we have obtained high resolution ( $2''$ ) interferometric CO maps, we need to resolve the SF activity and estimate the SFR within the radius ( $R_{\text{CO}}$ ), which encompasses most of the detected CO emission. We denote this as  $\text{SFR}_{\text{CO}}$ . We can then verify whether the large range in  $\text{SFR}/M_{\text{H}_2}$  seen within the sample when using  $45''$  averaged data persists even at higher resolution.  $R_{\text{CO}}$  is estimated by determining where the azimuthally averaged gas surface density falls below a few % of its peak value, and ranges from 500 to 1680 pc (Table 8).

We estimate  $\text{SFR}_{\text{CO}}$  within  $R_{\text{CO}}$  by considering an ensemble of SFRs derived from different tracers which each may offer a different advantage in terms of resolution, apertures, and extinction. For instance, a well-established physical framework exists linking H $\alpha$  recombination lines to the UV continuum photons from massive young stars (e.g., Kennicutt 1998), but H $\alpha$  fluxes can be strongly affected by extinction in the dusty circumnuclear region where gas densities reach several 100 to  $1000 M_{\odot} \text{ pc}^{-2}$ . Conversely, tracers such as the far-infrared or RC luminosity are less affected by extinction, but have lower spatial resolution such that they may not always resolve the SF within  $R_{\text{CO}}$ .

Following Condon (1992) and Kennicutt (1998), we estimate in sections (i) to (iii) the SFRs from the global FIR luminosity, the Br $\gamma$  luminosity, the non-thermal and thermal components of the RC emission which we denote, respectively, as  $\text{SFR}_{\text{FIR}}$ ,  $\text{SFR}_{\text{Br}\gamma}$ ,  $\text{SFR}_{\text{RC-N}}$ , and  $\text{SFR}_{\text{RC-T}}$ . Table 7 summarizes the values and apertures for each tracer.

(i) *SFR based on the the global FIR luminosity ( $SFR_{\text{FIR}}$ ):* The global FIR luminosity traces the massive SFR over the entire galaxy, under the assumption that most of FIR emission between 40 and 120  $\mu\text{m}$  emanates from warm dust heated by massive stars.  $SFR_{\text{FIR}}$  was computed from

$$\left(\frac{\text{SFR}}{M_{\odot}\text{yr}^{-1}}\right) = 4.3 \times \text{SFR}(M \geq 5M_{\odot}) = \gamma \times \left(\frac{L_{\text{FIR}}}{10^{10}L_{\odot}}\right) \quad (5)$$

where SFR ( $M \geq 5M_{\odot}$ ) is the rate of formation of stars with mass  $M \geq 5M_{\odot}$ . An extended Miller-Scalo IMF (Kennicutt 1983) with an upper mass cut-off  $M_{\text{U}}$  of 100  $M_{\odot}$  is assumed. We adopt  $\gamma = 3.9$  (Condon 1992). As shown in Table 7, the global SFR ranges from 6 to 14  $M_{\odot}\text{yr}^{-1}$  for the starbursts and from 0.2 to 4  $M_{\odot}\text{yr}^{-1}$  for the non-starbursts. These values apply to the entire galaxy and therefore serve as an upper limit to the SFR in the circumnuclear region.

(ii) *SFR based on the non-thermal and thermal component of the RC emission ( $SFR_{\text{RC-N}}$ ,  $SFR_{\text{RC-T}}$ ):* The thermal free-free emission from the photoionized HII regions and the non-thermal RC emission produced by relativistic electrons which are accelerated by supernova remnants are both related to the massive SFR. The RC flux density at 1.5 and 4.9 GHz is dominated by non-thermal emission. We estimate the non-thermal fraction to be 0.88 at 1.5 GHz and 0.77 at 4.9 GHz following the approximation by Condon & Yin (1990) :

$$\left(\frac{S}{S_{\text{T}}}\right) = 1 + 10 \times \left(\frac{\nu}{\text{GHz}}\right)^{0.1-\alpha} \quad (6)$$

where the non-thermal index  $\alpha$  is  $\sim 0.8$ . From the non-thermal component of the RC luminosity density ( $L_{\text{N}\nu}$ ), we estimate the star formation rate  $SFR_{\text{RC-N}}$  within the radius  $R_{\text{RC}}$  using

$$\left(\frac{SFR_{\text{RC-N}}}{M_{\odot}\text{yr}^{-1}}\right) = 4.3 \times 0.019 \times \left(\frac{\nu}{\text{GHz}}\right)^{\alpha} \left(\frac{L_{\text{N}\nu}}{10^{20}\text{WHZ}^{-1}}\right) \quad (7)$$

This equation assumes the Galactic relationship between the supernova rate and the RC luminosity density (Condon 1992). As shown in Table 7,  $SFR_{\text{RC-N}}$  applies to the region of radius  $R_{\text{RC}}$  which covers the inner 1-2 kpc, except for NGC 3359 and NGC 4314 where larger apertures apply.  $SFR_{\text{RC-N}}$  ranges from 3 to 14  $M_{\odot}\text{yr}^{-1}$  for the starbursts and from 0.1 to 2  $M_{\odot}\text{yr}^{-1}$  for the non-starbursts. When estimating SFRs in NGC 6951, we excluded the luminosity contribution from the inner 100 pc radius to avoid contamination from the Seyfert nucleus that is known to exist from optical line ratios (Munoz-Tunon et al. 1989)

We estimate the SF rate ( $SFR_{\text{RC-T}}$ ) from the thermal component of the RC emission ( $L_{\text{T}\nu}$ ) using

$$\left(\frac{SFR_{\text{RC-T}}}{M_{\odot}\text{yr}^{-1}}\right) = 4.3 \times 0.176 \times \left(\frac{L_{\text{T}\nu}}{10^{20}\text{WHZ}^{-1}}\right) \times \left(\frac{T_{\text{e}}}{10^4\text{K}}\right)^{-0.45} \left(\frac{\nu}{\text{GHz}}\right)^{0.1} \quad (8)$$

$SFR_{\text{RC-T}}$  is slightly lower than  $SFR_{\text{RC-N}}$ , but the difference is only at the 5 % level. It is encouraging that the

same trend is seen in estimates based on radio continuum ( $SFR_{\text{RC-N}}$ ) and FIR ( $SFR_{\text{FIR}}$ ) light: the starbursts have larger SFRs (3 to 14  $M_{\odot}\text{yr}^{-1}$ ) than the non-starbursts (0.1 to 2  $M_{\odot}\text{yr}^{-1}$ ). Figure 4 shows  $SFR_{\text{RC-N}}$  plotted against  $SFR_{\text{FIR}}$ .  $SFR_{\text{RC-N}}$  is comparable to  $SFR_{\text{FIR}}$  in all galaxies except NGC 2782 and NGC 3504, where  $SFR_{\text{RC-N}}$  is 10 to 30 % higher. This could be caused by a variety of reasons. The dust temperature and emissivities could be different from those assumed such that  $SFR_{\text{FIR}}$  underestimates the true global SFR. Another possibility is that part of the non-thermal RC emission is coming from starburst-driven outflows, where the empirical Galactic relationship between the supernova rate and the RC luminosity density might not hold. In fact, in NGC 2782, the high (1'') resolution RC map (Saikia et al. 1994) shows that a large fraction of the RC emission emanates from double outflow shells which extend 850 pc away from the central starburst (Jogee et al. 1998). Furthermore, while there is no evidence from optical line ratios for an active nucleus in these two galaxies, one cannot rule out the possibility that part of the non-thermal RC emission may be due to a hidden active nucleus.

(iii) *SFR based on Br $\gamma$  fluxes ( $SFR_{\text{Br}\gamma}$ ):* The Br $\gamma$  recombination line at 2.16  $\mu\text{m}$  traces Lyman continuum photons from massive stars. Published Br $\gamma$  fluxes (e.g., Puxley et al. 1990) are only available for four starbursts NGC 2782, NGC 3504, NGC 4102, and NGC 4536 and for the non-starburst NGC 3351. As shown in Table 7, the radius  $R_{\text{Br}\gamma}$  of the region over which Br $\gamma$  observations were made varies between 500 to 1600 pc depending on the galaxy.  $SFR_{\text{Br}\gamma}$  is 1 to 6  $M_{\odot}\text{yr}^{-1}$  for the starbursts and 0.5  $M_{\odot}\text{yr}^{-1}$  for the non-starburst NGC 3351, as computed from :

$$\left(\frac{\text{SFR}}{M_{\odot}\text{yr}^{-1}}\right) = 11.97 \times 10^{-54} \left(\frac{N_{\text{Ly}}}{\text{s}^{-1}}\right) \quad (9)$$

$SFR_{\text{RC-N}}$  is larger by a factor of 2 to 5 compared to  $SFR_{\text{Br}\gamma}$  in NGC 2782, NGC 3504, NGC 4102, and NGC 4536, where both SF rates are measured over comparable radii. It is likely that  $SFR_{\text{Br}\gamma}$  underestimates the true SFR as the Br $\gamma$  data and ionization rate ( $N_{\text{Ly}}$ ) quoted by Puxley et al. (1990) have not been corrected for extinction at 2.2  $\mu\text{m}$ . Dust within an internally dusty HII region can absorb Lyman continuum photons before they ionize any H atom, and dust along the line of sight can absorb part of the Br $\gamma$  recombination photons.

Table 7 summarizes the SFR estimated ( $SFR_{\text{FIR}}$ ,  $SFR_{\text{Br}\gamma}$ ,  $SFR_{\text{RC-N}}$ , and  $SFR_{\text{RC-T}}$ ) from these tracers and the aperture over which it applies. From these values, we make a best estimate for  $SFR_{\text{CO}}$ , the extinction-corrected SFR within the radius ( $R_{\text{CO}}$ ) over which CO emission is detected in the moment maps. In the case of NGC 470, NGC 2782, NGC 4102, NGC 4536, and NGC 4569, we consider  $SFR_{\text{RC-N}}$  to be a reasonable estimate for  $SFR_{\text{CO}}$  since the RC maps show that most of the RC emission is concentrated within  $R_{\text{CO}}$ . For the remaining galaxies NGC 3504, NGC 3351, and NGC 4314, ( $R_{\text{RC}}/R_{\text{CO}}$ ) is 0.6, 1.7, and 6.0 respectively. In NGC 3504,  $SFR_{\text{RC-N}}$  is a reasonable approximation for the SF rate within  $R_{\text{CO}}$  (1300 pc) because the H $\alpha$  map shows that more than 90 % of H $\alpha$  flux within  $R_{\text{CO}}$  originates from the inner 800 pc radius. In the case of NGC 3351,  $R_{\text{CO}}$  is

$\sim 600$  pc, which is close to  $R_{\text{Br}\gamma} \sim 500$  pc. We therefore adopt  $\text{SFR}_{\text{CO}}$  as  $0.5 M_{\odot} \text{ yr}^{-1}$  based on the  $\text{Br}\gamma$  estimates. In the case of NGC 4314, we consider  $\text{SFR}_{\text{RC-N}} \sim 0.1 M_{\odot} \text{ yr}^{-1}$  within  $R_{\text{RC}} \sim 3600$  pc as an upper limit to the SF rate within  $R_{\text{CO}} \sim 600$  pc.

Table 8 shows the resulting  $R_{\text{CO}}$ ,  $\text{SFR}_{\text{CO}}$  and the mass of molecular hydrogen ( $M_{\text{H}_2}$ ) within this radius. The resulting *circumnuclear SFR ranges from 3 to 11  $M_{\odot} \text{ yr}^{-1}$  in the starbursts and from 0.1 to 2  $M_{\odot} \text{ yr}^{-1}$  in the non-starbursts.* It is evident that while non-starbursts such as NGC 4569 and NGC 6951 and starbursts such as NGC 4102, NGC 4536, and NGC 2782 all host several times  $10^9 M_{\odot}$  of molecular hydrogen, their SFRs are substantially different. A similar comparison applies between the starburst NGC 470 and the non-starbursts NGC 3351 and NGC 4314 which host several times  $10^8 M_{\odot}$  of molecular hydrogen.

## 8. COMPARISON OF MOLECULAR GAS IN THE STARBURSTS AND NON-STARBURSTS

Table 8 shows that *barred galaxies with comparable amount of molecular gas in the inner 1-2 kpc radius can show an order of magnitude range in the average SFR per unit mass of gas ( $\text{SFR}/M_{\text{H}_2}$ ) within this region.* Among galaxies which host several times  $10^9 M_{\odot}$  of molecular hydrogen in the inner 2 kpc, starbursts such as NGC 4102, NGC 4536, and NGC 2782 have an average ( $\text{SFR}/M_{\text{H}_2}$ ) of order a few times  $10^{-9} \text{ yr}^{-1}$  while non-starbursts NGC 4569 and NGC 6951 have ( $\text{SFR}/M_{\text{H}_2}$ )  $\sim$  a few  $\times 10^{-10} \text{ yr}^{-1}$ . We now turn to a comparison of the circumnuclear molecular gas in the barred starbursts and non-starbursts with the overall goal of understanding why they have such different SFR per unit mass of gas ( $\text{SFR}/M_{\text{H}_2}$ ) in the inner few kpc.

While we focus here on a comparison of the starbursts and non-starbursts (Figs. 3,5,6,7), we refer any interested reader to § 11 for a description of each *individual* galaxy. Figures 3a–b show a wide variety of molecular gas morphologies including relatively axisymmetric annuli or disks (starbursts NGC 4102, NGC 3504, NGC 4536, NGC 470, and non-starburst NGC 4314), elongated double-peaked and spiral morphologies (starburst NGC 2782 and non-starbursts NGC 3351 and NGC 6951), and highly extended distributions (non-starburst NGC 4569) In all of the sample galaxies (Figs. 3a–b) except for the non-starburst NGC 4569, the molecular gas is concentrated in the inner kpc radius. Figure 5 compares the spatial distribution of SF activity (shown as greyscale) and molecular gas (shown as CO contours). The x and y axes represent respectively,  $M_{\text{H}_2}$  and ( $\text{SFR}/M_{\text{H}_2}$ ), as defined in Table 8. In the case of NGC 4102, NGC 2782 and NGC 6951, we show the SF activity with existing high resolution ( $1.0''$ – $1.5''$ ) 1.49 and 4.89 GHz RC maps. Strictly speaking, in the case of NGC 6951, the RC map shows not just the star-forming ring of  $4''$  (360 pc) radius, but also the Seyfert nucleus in the inner  $1''$  (90 pc). For the remaining galaxies in Fig. 5, we use high resolution ( $1.0''$  –  $1.5''$ )  $\text{H}\alpha$  maps as there are no RC maps of resolution comparable to the CO. Our conclusions are given below.

### 8.1. The Type I Non-Starburst NGC 4569

The non-starburst NGC 4569 differs from the other sample galaxies in that it has a highly extended molecular gas distribution with complex kinematics and large linewidths of  $\sim 150 \text{ km s}^{-1}$ . These properties of NGC 4569 are illustrated in Figs. 6a–d. A large fraction of the gas lies outside the inner kpc radius and extends out to a radius of  $20''$  (1.7 kpc), at a similar P.A. ( $\sim 15$  deg) as the large-scale stellar bar (Figs. 6a–b). The extended gas in NGC4569 has highly non-circular kinematics, as shown by the p-v plots along the kinematic major and minor axes (Figs. 6c–d). Along the kinematic major axis, velocities are generally positive (i.e., above the systemic value of  $-235 \text{ km s}^{-1}$ ) on the northeastern side, and negative on the southwest side. However, at a radius of  $5''$  (400 pc), near the feature marked ‘N1’ in Fig. 6b, the velocities change from  $+100 \text{ km s}^{-1}$  to a forbidden velocity of  $-75 \text{ km s}^{-1}$ . This indicates the presence of non-circular motions caused by in-plane azimuthal streaming motions or/and vertical motions out of the plane.

As outlined in § 2.2, NGC 4569 shows signs of optical and NIR asymmetries suggestive of a recent tidal interaction or minor merger and it also hosts a large-scale stellar bar. Thus, we suggest that the extended gas in NGC 4569 which is generally elongated along the bar and shows strong streaming motions, is responding to gravitational torques from both the interaction and the (induced or spontaneous) stellar bar. *Taken together, the optical, NIR, and CO properties of NGC 4569 suggest it is in the early phases of bar-driven/tidally-driven gas inflow.* NGC 4569 is reminiscent of NGC 7479 which hosts large amounts of gas with non-circular kinematics along a large-scale stellar bar and show evidence for a minor merger (Laine & Heller 1999). However, the gas kinematics in NGC 4569 look more disturbed in the inner 400 pc than in NGC 7479.

There is intense SF in the central  $2''$  (170 pc) radius, but the gas which is extended along the bar and has disturbed kinematics shows no appreciable SF. The properties of NGC 4569 stand in sharp contrast to the starburst NGC 4102, where most of the circumnuclear molecular gas has piled up in the inner  $4''$  (340 pc) radius, shows predominantly circular kinematics, and is undergoing intense SF. The low SF efficiency in NGC 4569 is likely related to the fact that large velocity gradients and shear in gas streaming along the bar can prevent clouds from being self-gravitating. Additionally, gas moving in a bar potential can experience large tidal forces (Elmegreen 1979; Kenney & Lord 1991) and tidal heating (Das & Jog 1995) which slow down gravitational collapse. Several other galaxies show such low SF per unit mass of gas along their bars e.g., NGC 7723 (Chevalier & Furenlid 1978), NGC 1300, NGC 5383 (Tubbs 1982), NGC 7479 (Laine et al. 1999) or in M83 where the ratio of UV to CO luminosities is unusually low despite abundant CO (Handa, Sofue, & Nakai 1991).

In summary, we therefore suggest that the low SFR per unit gas mass of the non-starbursts NGC 4569 over the inner few kpc is due to the fact that *it is in the early stages of bar-driven/tidally-driven gas inflow, where most of its molecular gas has an extended distribution, highly non-circular kinematics and an associated large local shear which is not conducive to SF.* The barred galaxy NGC 7479 studied by Laine et al. (1999) may also be in this

early evolutionary phase. In NGC 7479, only low levels of SF are seen along the bar despite the presence of several  $\times 10^9 M_{\odot}$  of molecular gas in a dust lane along the bar (Laine et al. 1999). This gas shows large non-circular motions, a large velocity gradient, and a projected velocity gradient of at least  $100 \text{ km s}^{-1}$  (Laine et al. 1999). We shall henceforth use the term ‘**Type I non-starburst**’ to denote this kind of system, where a large fraction of the molecular gas is still inflowing toward the inner kpc, along the leading edges of the bar, exhibiting large non-circular motions and not forming stars efficiently.

### 8.2. The Starbursts and Type II Non-Starbursts

The remaining starbursts (NGC 4102, NGC 3504, NGC 4536, NGC 470) and non-starbursts (NGC 6951, NGC 3351, NGC 4314) in our sample do not show such extreme kinematics or extended gas distributions as NGC 4569. In all of them, the molecular gas detected is concentrated within the inner kpc radius and the velocity field in the inner 500 pc radius is generally dominated by circular motions, with occasional weaker non-circular components (see § 11 for details). Most of the circumnuclear molecular gas seems to have reached the inner kpc radius of the bar and only a small fraction of it seems to be still inflowing along the stellar bar. The latter gas component shows up in the form of faint gas streams which extend out and intersect the dust lanes on the leading edges of the large-scale bar and show non-circular motions. Such gas streams are seen in clearly in non-starburst NGC 6951 (Fig. 15a–b) and also at fainter levels in NGC 3351 (Fig. 15c–d), NGC 4314 (Fig. 15e–f), and starburst NGC 4102 (Fig. 14a–b). We conclude that in contrast to NGC 4569, the remaining barred starbursts and non-starbursts seem to be *in significantly later stages of bar-driven inflow where most of the molecular has already settled into the inner kpc of the barred potential and no longer shows extreme non circular motions*. We henceforth refer to these kind of non-starbursts as ‘**Type II non-starbursts**’.

What is the difference between the starbursts and Type II non-starbursts? To answer this question, we use the two-dimensional distribution of SF and gas in Fig. 5, as well as the azimuthally averaged gas and SFR surface densities in Fig. 7a–b. Fig. 7a shows the radial variation of the deprojected azimuthally-averaged molecular gas surface density ( $\Sigma_{\text{gas-m}}$ ) derived in § 5. In order to display meaningful values, quantities are plotted starting at a radius  $\geq$  half the size of the synthesized CO beam which is typically  $2''$  or 150 pc. Fig. 7b plots the azimuthally-averaged molecular gas surface density SFR per unit area ( $\Sigma_{\text{SFR}}$ ) in the galactic plane as a function of radius. We find that the starbursts show larger gas surface densities ( $1000\text{-}3500 M_{\odot} \text{ pc}^{-2}$ ) in the inner 500 pc radius compared to the Type II non-starbursts for a given CO-to- $\text{H}_2$  conversion factor. In Fig. 7a, the Type II non-starbursts have peak  $\Sigma_{\text{gas-m}}$  reaching only  $500\text{-}950 M_{\odot} \text{ pc}^{-2}$ . We also note from Fig 6a and 6b that in the central 600 pc radius,  $\Sigma_{\text{gas-m}}$  and  $\Sigma_{\text{SFR}}$  follow each other more closely in the case of the starbursts.

Is the presence of apparently higher gas surface densities in the starbursts a real effect? We can rule out artifacts caused by resolution effects since we have similar linear resolution (in pc) for starbursts and non-starbursts with com-

parable circumnuclear molecular gas content (e.g., NGC 4102, and NGC 3504 versus NGC 6951, or NGC 2782 and NGC 4536 versus NGC 4569). Another concern is that the higher  $\Sigma_{\text{gas-m}}$  in the starbursts may be due to an increase in CO emissivity caused by the higher temperatures associated with the intense SF. However, potential variations in CO emissivity cannot account for the observed differences in  $\Sigma_{\text{gas-m}}$  since CO peaks do not coincide with the  $\text{H}\alpha$  and RC peaks in several galaxies e.g., NGC 6951, NGC 2782, and NGC 3351 (Fig. 5). Thus, the starbursts appear to have an intrinsically larger molecular gas surface density in the central 500 pc than the non-starbursts. This difference of a factor of 3–4 in  $\Sigma_{\text{gas-m}}$  can in turn lead to large differences in the SF *if gas in the starbursts is above a critical density for SF while a large part of the gas in the non-starbursts is sub-critical*. We address this possibility quantitatively in § 9 by comparing  $\Sigma_{\text{gas-m}}$  to different theoretical critical densities which are believed to be relevant for the onset of SF.

### 9. THEORETICAL MODELS FOR SF APPLIED TO CIRCUMNUCLEAR STARBURSTS AND TYPE II NON-STARBURSTS

We compare the observed circumnuclear gas surface density  $\Sigma_{\text{gas-m}}$  to the critical density relevant for the onset of SF with the overall goal of understanding some of the differences between the starbursts and Type-II non-starbursts. In particular, we consider theoretical scenarios which assume that the onset of gravitational or axisymmetric instabilities (Safronov 1960; Toomre 1964; Goldreich & Lynden-Bell 1965a; Elmegreen 1979) is relevant for the growth of clouds and the onset of SF. Such models have achieved a fair degree of empirical success in the outer disks of Sa-Sc spirals, gas-rich E and S0s s (Kennicutt 1989; Eder 1990; Kennicutt 1998b). Extensions of such models to include magneto-Jeans instabilities have also been developed (Kim et al. 2002).

For a thin differentially rotating gas disk, support against gravitational instabilities is provided by pressure forces on small scales, and by Coriolis forces from rotation on large scales. One can show that axisymmetric instabilities set in when the gas surface density  $\Sigma_{\text{gas}}$  exceeds a critical density such that the Safronov (1960)/Toomre (1964)  $Q$  parameter falls below 1, where

$$Q = \frac{\Sigma_{\text{crit}}}{\Sigma_{\text{gas}}} = \frac{\alpha \kappa \sigma}{\pi G \Sigma_{\text{gas}}} \leq 1 \quad (10)$$

Here,  $\omega$  is the angular frequency,  $\Sigma_{\text{gas}}$  is the gas surface density,  $\sigma$  is the gas velocity dispersion,  $\kappa$  is the epicyclic frequency, and  $G$  is the gravitational constant. For an infinitely thin disk,  $\alpha$  is 1, but for disks of finite thickness,  $\alpha$  is somewhat larger (Larson 1985). Empirically, Kennicutt (1989) found that  $\alpha$  is  $\sim 0.7$  in the outer disks of Sc spirals. A two-fluid disk made of both gas and stars is always more unstable and will have a lower  $\alpha$  than a purely gaseous or stellar one-fluid disk (Jog & Solomon 1984; Elmegreen 1995).

We discuss the gravitational instability models in the context of the type II non-starbursts NGC 4314, NGC 3351, and NGC 6951, and the starbursts NGC 4102, NGC 4536 and NGC 3504. We cannot apply these simply axisymmetric models to other sample galaxies as they have

highly non-axisymmetric gas distributions (e.g., the starburst NGC 2782 and Type I non-starburst NGC 4569) and non-circular kinematics (e.g., NGC 4569). We ignore the contribution of atomic HI because we have limited high resolution HI data for our sample galaxies and furthermore, molecular hydrogen is believed to dominate the ISM in the inner kpc of spirals (e.g., Scoville & Sanders 1987; Tacconi & Young 1986).

A more vicious problem is to get a good estimate for the velocity dispersion  $\sigma$  in the central ( $2''$ ), especially when the  $2''$  CO beam encompasses a steeply rising rotation curve. In the latter case, beam smearing artificially increases the observed  $\sigma$  and to a lesser degree impacts  $\kappa$  and  $\Sigma_{\text{gas}}$  in ways that depend on the intrinsic intensity and velocity field (Jogee 1999). Given that corrections for beam-smearing are model-dependent and not necessarily unique, we decide not to apply any such corrections, and instead perform the instability analyzes (Fig. 8) only for radii exceeding  $2''$  where the effect of beam-smearing is much less severe. In non-starbursts and starbursts alike, we therefore present results over radii of  $\sim 2''$ – $8''$  (Fig. 8). The lower limit of  $2''$  corresponds to 180 pc for NGC 6951, NGC 4102 and NGC 4536, and to 100 pc for NGC 4314 and NGC 3351. Our results are summarized below.

**(i) Type II non-starburst NGC 4314:** In NGC 4314, HII regions are concentrated within an annulus between a radius of  $5''$  and  $7''$  (240 and 400 pc) where  $\Sigma_{\text{gas}}$  is  $\sim 800 M_{\odot} \text{pc}^{-2}$  (Fig. 8). Interior to this annulus, there are no HII regions although  $\Sigma_{\text{gas}}$  drops by only a factor of 2-3 (Fig 8). This lack of SF activity is not an artifact caused by extinction in the  $H\alpha$  image or by resolution effects since neither the  $J$ - $K$  image (Friedli et al. 1996) nor the high resolution  $HST$  images (Benedict et al. 1996) show elevated levels of dust or young stars at  $r < 250$  pc. Thus, SF appears truly suppressed interior to the annulus of HII regions. The instability analysis (Fig. 8) shows that  $Q$  reaches its lowest value, between 1 and 2, in the star-forming annulus between  $r=5''$  and  $7''$  (240 and 400 pc) and it rises sharply at lower and higher radii. At  $r \geq 7''$  where we cannot measure  $\sigma$ , we adopted a lower limit of  $10 \text{ km s}^{-1}$  based on the fact that a relatively constant value of 10 to  $6 \text{ km s}^{-1}$  has been measured in the outer disks of spirals (e.g., Dickey et al. 1990). Thus, values estimated for  $Q$  at  $r \geq 7''$  outside the SF annulus are lower limits and the true rise in  $Q$  is likely to be even sharper than shown in Fig. 8. Interior to the star-forming annulus, between  $r = 2''$  and  $5''$  (100 to 240 pc),  $Q$  increases by more than a factor of 3, indicating highly sub-critical gas densities. It is unlikely that this rise in  $Q$  is primarily due to beam-smearing because the observed  $\sigma$  increases by at most 1.5 interior to the SF annulus. (The mean value of  $\sigma = 25 \text{ km s}^{-1}$  inside the SF ring and  $15 \text{ km s}^{-1}$  in the ring).

**(ii) Type II non-starburst NGC 3351:** In NGC 3351, the SF activity is concentrated within an annulus between a radius of  $6''$  and  $9''$  (300 and 450 pc) where  $\Sigma_{\text{gas}}$  is  $\sim 550 M_{\odot} \text{pc}^{-2}$  (Fig. 8). At lower radii, between  $2''$  and  $6''$  (100 and 450 pc), there is a large amount of molecular gas and  $\Sigma_{\text{gas}}$  shows no significant change. Yet no HII regions are seen (Fig. 8). The absence of observed SF activity at  $r < 6''$  is not caused by extinction since near-infrared

$K$ -band observations of NGC 3351 show several hot spots (likely due to young  $K$  supergiants) in the ring of HII regions, but a relatively smooth distribution suggestive of older stars further in (Elmegreen et al. 1997). We find that in NGC 3351  $Q$  reaches its minimum value of  $\sim 1.5$  in the annulus of HII regions between a radius of  $6''$  and  $9''$  (300 and 450 pc; Fig 8). Further in, between a radius of  $2''$  and  $6''$  (100 and 450 pc),  $Q$  rises sharply to  $\sim 6$  suggesting sub-critical gas densities. We again note that this increase in  $Q$  by a factor of  $> 3$  is not primarily due to beam-smearing since the observed  $\sigma$  does not show a similar increase.  $\sigma$  has a mean value of  $20 \text{ km s}^{-1}$  in the SF ring and  $25 \text{ km s}^{-1}$  inside it.

**(iii) Type II non-starburst NGC 6951:** In NGC 6951, a similar trend in the  $Q$  parameter exists. The massive CO peaks at a radius of  $6''$  (550 pc) host a local molecular gas surface density of  $2000 M_{\odot} \text{pc}^{-2}$  and an azimuthally averaged  $\Sigma_{\text{gas}}$  of  $1000 M_{\odot} \text{pc}^{-2}$  (Fig. 8). Yet, the CO peaks are not associated with SF either in  $H\alpha$  and RC maps. Instead, SF is concentrated in a ring of radius  $\sim 3''$  (300 pc). Kohno et al. (1999) find that  $Q$  is close to 1 in the star-forming annulus.

**(iv) The starbursts NGC 4102, NGC 4536:** The circumnuclear SF in the starbursts NGC 4102 and NGC 4536 is distributed over a wide annulus between 100 and 700 pc. Although the ground-based  $H\alpha$  or RC images (e.g., Fig. 5) may give the misleading impression that SF extends all the way into the center,  $HST$  images of both galaxies show a smooth distribution of old stars within the central 100 pc ( $1''$ ) radius. Adopting the same approach for the starbursts NGC 4102 and NGC 4536 as for the non-starbursts, we perform the instability analysis from  $r \sim 2''$ – $8''$  (Fig. 8). As before, we exclude the central  $r \sim 2''$  radius where the effect of beam smearing is severe. We also exclude larger radii ( $r > 8''$ ) where there are faint gas streams which connect to the large-scale dust lanes on the leading edges of the bar because the Toomre analysis is not valid for such non-axisymmetric gas distributions.

The instability analysis (Fig. 8) shows that in the starbursts NGC 4102 and NGC 4536, the Toomre  $Q$  parameter remains  $\sim 1$ -2 from  $r \sim 2''$ – $8''$  (200–700 pc) in the region of SF despite a factor of 2–3 variation in  $\sigma$  and a factor of 10 variation in both the gas surface density ( $\Sigma_{\text{gas}}$ ) and the epicyclic frequency ( $\kappa$ ). Indeed, between a radius of 200 and 700 pc,  $\sigma$  ranges from 40 to  $15 \text{ km s}^{-1}$ ,  $\Sigma_{\text{gas}}$  from 2200 to  $200 M_{\odot} \text{pc}^{-2}$ , and  $\kappa$  from 1500 to  $200 \text{ km s}^{-1} \text{kpc}^{-1}$ . A value of  $Q \sim 1$  is also found in the starburst NGC 3504 by Kenney et al (1993). Furthermore, inspection of Fig. 8 shows that the  $Q \sim 1$ -2 annulus spans  $\sim 450$  pc (e.g., 250–700 pc) in the starbursts NGC 4102 and NGC 4536, but only  $\sim 150$  pc (e.g., 300–450 pc) in the non-starbursts NGC 4314 and NGC 3351. It thus appears that the annulus over which  $Q$  remains  $\sim 1$ -2 is 3 times wider in the starbursts than in the non-starbursts suggesting that the former host a larger amount of gas which is close to the critical density.

**(v) Overall trends:** The analyzes in § (i)–(iv) suggest that the Toomre  $Q$  parameter remains  $\sim 1$ -2 in the region of SF despite the large dynamic range in molecular gas properties, namely a factor of a few variation in  $\sigma$  and an order of magnitude variation in the gas surface

density ( $\Sigma_{\text{gas}}$ ) and the epicyclic frequency ( $\kappa$ ). It is true that the analyzes involve many uncertain quantities such as the CO-to-H<sub>2</sub> conversion factor and should, therefore, be taken with a grain of salt. However, with such a large variation in quantities such as  $\Sigma_{\text{gas}}$  and  $\kappa$ ,  $Q$  could easily have ended up having almost any value, and the fact that it remains close to 1 can hardly be fortuitous. Instead, the evidence presented strongly suggests that the onset of gravitational instabilities as characterized by  $Q$  plays an important role in controlling the onset of SF in the inner kpc of spirals. At first sight, this may seem surprising since large-scale gravitational instabilities have been invoked for the collapse of atomic gas into molecular clouds within the outer disk of galaxies, but molecular gas in the inner kpc is already in the form of clouds. However, large-scale gravitational instabilities may be relevant for SF even in the inner kpc because they help to aggregate molecular clouds into large complexes where the clouds can thereafter grow through local processes involving accretion and collisions (e.g., Kwan 1979; Scoville et al. 1986; Gammie, Ostriker, & Jog 1991; Elmegreen 1990).

The results presented in § (i)–(iv) also suggest at least a partial explanation for the differences in SFR per unit mass of gas between the non-starbursts and starbursts. In both Type II non-starbursts and starbursts, the  $Q$  parameter reaches its minimum value of  $\sim 1$ – $2$  in the annuli of SF. However, the annulus over which  $Q$  remains  $\sim 1$ – $2$  is three times wider in the starbursts than in the non-starbursts, suggesting that *starbursts host a larger amount of gas which is close to the critical density*. Inside and outside the annuli of SF, the Type II non-starbursts host large gas concentrations where gas densities are well below  $\Sigma_{\text{crit}}$  ( $Q \gg 2$ ), and SF appears inhibited.

## 10. BAR PATTERN SPEEDS AND DYNAMICAL RESONANCES OF THE BAR

A barred potential is made up of different families of periodic stellar orbits characterized by a (conserved) Jacobi energy,  $E_J$ , a combination of energy and angular momentum (e.g., Binney & Tremaine 1987). The most important families are those aligned with the bar major axis (so-called  $x_1$  orbits) or with its minor axis ( $x_2$  orbits) (Contopoulos & Papayannopoulos 1980). The  $x_1$  family extends between the center and the bar’s corotation radius. If the central mass concentration of a bar is large enough, it can also develop one or more inner Lindblad resonances (ILRs). The exact locations and even the number of ILRs can be inferred reliably from non-linear orbit analysis (e.g., Heller & Shlosman 1996) based on the knowledge of the galactic potential. The abrupt change in orientation by  $\pi/2$  at each resonance is restricted to (collisionless) stellar orbits. The gas-populated orbits can change their orientation only gradually due to shocks induced by the finite gas pressure. The gas response to bar torquing leads to the formation of large-scale offset shocks and a subsequent gas inflow. The latter stalls in the inner few 100 pc because shocks associated with the bar weaken, and gravitational torques in the vicinity of ILRs may even reverse (e.g., Combes & Gerin 1985; Shlosman et al. 1989; Athanassoula 1992).

Here we use the CO, optical, and NIR data of the sample galaxies to constrain two fundamental properties of their

stellar bar: its pattern speed ( $\Omega_p$ ) and the location of its dynamical resonances. The pattern speed influences the interaction of the bar with the dark matter halo (e.g., Debattista & Sellwood 2000; Athanassoula 2002; Berentzen, Shlosman, & Jogee 2005) and the location of its resonances. We use two empirical methods: (I) *Kinematic method based on the epicyclic approximation*: For a weak bar, the potential can be expressed as the linear sum of an axisymmetric term and a smaller non-axisymmetric term, and epicycle theory can be used to solve for the equations of motion of a star. In such a case, simple relationships exist between the location of its resonances and dynamical frequencies, such as  $\Omega_p$ ,  $\Omega$ , and  $\kappa$ . We derive  $\Omega$  and  $\kappa$  from the CO and H $\alpha$  rotation curves as described in § 5, bearing in mind that uncertainties exist in regions where there are non-circular motions. We fit ellipses to the NIR and optical images in order to estimate the location of the bar end (e.g., Jogee et al. 1999; 2004a). Next, we set upper limits on the pattern speed  $\Omega_p$  by assuming that a bar ends inside or at the corotation resonance (CR), where  $\Omega = \Omega_p$ . This widely used assumption is justified by the fact that between the ultra-harmonic resonance and CR, chaotic orbits dominate, while beyond the CR, the orbits become aligned perpendicular to the bar. We derive upper limits on  $\Omega_p$  in the range of 43 to 115 km s<sup>-1</sup> kpc<sup>-1</sup> across the sample (Table 9; Figs. 9a–b).

At the ILRs, there is a match between the natural frequency of radial oscillations ( $\kappa$ ), and the forcing frequency ( $\Omega - \Omega_p$ ),

$$\Omega - \Omega_p = \pm \kappa/2 \quad (11)$$

where  $\Omega$  is the angular frequency and  $\Omega_p$  is the bar pattern speed. For a weak bar, if the peak of  $(\Omega - \kappa/2)$  exceeds  $\Omega_p$  (Figs. 9a–b), then one or more ILRs must exist. This condition is satisfied in the starbursts NGC 4102, NGC 4536, and NGC 3504, and in the non-starbursts NGC 4314, NGC 6951, and NGC 3351. We use the upper limit on  $\Omega_p$  in Fig. 9a–b to derive lower and upper limits, respectively, for the radius of the OILR ( $R_{\text{OILR}}$ ) and IILR ( $R_{\text{IILR}}$ ). These are shown in Table 9.

(II) *Method based on the morphology of circumnuclear dust lanes*: In the presence of  $x_2$  orbits associated with ILRs, the two dust lanes which are associated with the leading edges of a bar do not cross the center of the galaxy, but are offset along the bar minor axis, in the direction of  $x_2$  orbits (e.g., Athanassoula 1992; Byrd et al 1994; Piner et al. 1995). The separation of the offset dust lanes provides a lower limit to  $2 \times R_{\text{OILR}}$ . Figs. 10a–c illustrate the case for the type II non-starburst NGC 6951. The large-scale stellar bar of NGC 6951 has a semi-major axis of 28'' (5.2 kpc; Fig. 10a) and two relatively straight dust lanes are visible on its leading edge (Fig. 10b). As they approach the circumnuclear region, these dust lanes do not cross the center of the galaxy, but instead are offset along the bar minor axis. These dust lanes connect to the spiral-shaped CO arms where the two CO peaks lie almost along the minor axis of the stellar bar (Fig. 10c) The CO and dust morphology are consistent with the accumulation of gas near the OILR. Similar pairs of offset dust lanes are seen in the starbursts NGC 3504 and NGC 4102, and in the type II non-starbursts NGC 3351 and NGC 4314.

A comparison of the lower limits on  $R_{\text{OILR}}$  (whether determined by method I or II) with the azimuthally-averaged

molecular gas surface density  $\Sigma_{\text{gas-m}}$  (Fig. 7a) shows that *the starbursts and Type II non-starbursts have their peak gas surface density and most of their circumnuclear gas inside or near the OILR of the stellar bar*. Similar results are reported in studies of individual systems (e.g., Kenney et al. 1992; Knapen 1995a,b; Jogee 1999, 2001; Jogee et al. 2002a,b). However, the CO data do not enable us to determine whether the gas has flown past the IILR since the CO resolution (100-200 pc) is comparable to the upper limits on  $R_{\text{IILR}}$ . However, we note that the *HST* images of many sample galaxies (e.g., NGC 4102, NGC 3504, NGC 4536, NGC 4314, NGC 3351, NGC 6951) show that SF does not extend inside the central 100 pc radius or so; this may be due to the IILR blocking further gas inflow. It is interesting that NGC 2782 which hosts a nuclear stellar bar (§ 11; Jogee et al. 1999) is the only starburst where *HST* images show the SF peaking at the center.

#### 11. BAR-DRIVEN SECULAR EVOLUTIONARY SCENARIOS

In this penultimate section, we discuss potential evolutionary connections between the barred starbursts and non-starbursts in our sample and how they fit into scenarios for bar-driven dynamical evolution.

The evidence presented in § 10 (based on the dynamical frequencies and dust morphologies) suggest that the starbursts and type II non-starbursts have piled up most of their circumnuclear gas inside or near the OILR of the large-scale stellar bar. In contrast, the Type I non-starburst such as NGC 4569 has an extended gas distribution extending out to  $r \sim 2$  kpc (§ 7), with a large fraction of the gas still inflowing along the bar and exhibiting large non-circular motions.

We suggest that a barred galaxy would show up as a Type I non-starburst in the early stages of bar-driven inflow where large amounts of gas are still along the bar, experiencing shocks, torques, and large non-circular motions. A schematic illustration is shown in Fig. 11. Examples of such systems might be NGC 4569 (§ 7; this work), NGC 7479 (§ 7; Laine et al. 1999), NGC 7723 (Chevalier & Furenlid 1978), NGC 1300, and NGC 5383 (Tubbs 1982). During this phase, SF is suppressed or highly inefficient due to large velocity gradients, shear, and tidal forces (Elmegreen 1979) in the gas along the bar. The low SFR/ $M_{\text{H}_2}$  along a strong bar, as typified by the Type I non-starburst, is fundamental in enabling a bar to efficiently increase the central mass concentration in the inner kpc of galaxies. It is only when the gas inflow rate along the bar exceeds the SFR over the same region, that an efficient mass buildup happens. Available estimates of gas inflow rates along large-scale stellar bars range from 1 to 4  $M_{\odot} \text{ yr}^{-1}$  (Quillen et al. 1995; Laine, Heller, & Shlosman 1998; Regan, Teuben, & Vogel 1997). If we assume a conservative net inflow rate of 1  $M_{\odot} \text{ yr}^{-1}$  along the bar into the inner kpc radius, then over 1 Gyr a bar can increase the dynamical mass in the inner kpc by  $1 \times 10^9 M_{\odot}$  or a few %. For instance, in our sample galaxies the dynamical mass (§ 5) enclosed within  $r=1$  kpc ranges from 6–30  $\times 10^9 M_{\odot}$  (Fig. 12), and would increase by 6–30 %. In practice, the mass buildup may be slower due to starburst-driven gas outflows which can be  $\sim 1$ –a few  $M_{\odot} \text{ yr}^{-1}$  (e.g., Jogee et al. 1998 for the starburst NGC 2782; Heckman, Armus, & Miley 1990).

As discussed in § 8 and 10, after gas crosses the OILR it settles into a more axisymmetric distribution with predominantly circular motions. Thus, in the later stages of bar-driven inflow, a barred galaxy is expected to become a Type II non-starburst (Fig. 11). The instability analysis in § 8 suggests that gas concentrations which build up near the ILRs will undergo SF once the gas densities exceed the Safronov (1960)/Toomre (1964) critical density  $\Sigma_{\text{crit}} = (\alpha\kappa\sigma/\pi G)$ . In the inner kpc, the very high epicyclic frequency (several 100–1000  $\text{km s}^{-1} \text{ kpc}^{-1}$ ) will naturally force  $\Sigma_{\text{crit}}$  to be high (e.g., several 100–1000  $M_{\odot} \text{ pc}^{-2}$ ), thereby enabling SF to occur only at high gas densities. Under this scenario, *some type II non-starbursts are pre-starbursts* which may eventually become starbursts (Fig. 11) if the gas density subsequently becomes super-critical.

The intense starbursts in our samples with circumnuclear SFRs of 3–11  $M_{\odot} \text{ yr}^{-1}$  will build compact young stellar disks or annuli inside the OILR. The interplay between the SFR, the outflow rate driven by starburst winds or jets, and the molecular gas supply will determine how massive such compact stellar components eventually will be. *These compact stellar components, which form from cold gas within the inner kpc, may belong to the class of so-called pseudo-bulges* (Kormendy 1993) whose light distribution and kinematics are more consistent with a disk than with a spheroidal bulge component. Several studies have in fact reported that the central light distribution of many late type galaxies are better represented by an exponential disk-like component than an  $r^{1/4}$  profile (e.g., de Jong 1996; Courteau, de Jong, & Broeils 1996)

As a typical starburst in our sample converts its molecular gas reservoir into such a compact disk-like stellar component, *it is expected to transition into a Type II non-starburst* as the gas density in part of the wide gas annulus will soon become sub-critical. One possible outcome is that SF shuts off first at lower radii (where  $\Sigma_{\text{crit}}$  is higher, the instability growth timescale  $t_{\text{GI}} \sim Q/\kappa$  is shorter, and  $\Sigma_{\text{SFR}}$  is higher) such that we end up with a newly-built compact disk-like stellar component lying inside a thin star-forming gas ring. In our own sample, the Type II non-starburst NGC 3351 may provide a striking example of this process. Inside its thin CO ring, NGC 3351 hosts a central stellar component which has a high ratio of rotational to random motions (Kormendy 1983) Isothermal fits to the *K* and *R* band images of NGC 3351 (Fig. 13) shows that this central component has an ellipticity and P.A similar to those of the outer disk. Both the light distribution and kinematics would suggest that a compact stellar component with disk-like properties has built up in the central  $r=6''$  (300 pc) of NGC 3351. Thus, in this framework *some Type II non-starbursts may also be post-starbursts hosting a compact disk-like stellar component* (Fig. 11). It should be noted that vertical instabilities (e.g., Sellwood 1993; Merritt & Sellwood 1994), vertical ILRs associated with the bars (Combes et al. 1990) can scatter stars in the initially flat disk component to large scale heights, thereby enhancing or building a stellar bulge.

The overall schematic picture (Fig. 11) which emerges is that an episode of bar-driven gas inflow causes a barred galaxy to go through successive phases from a Type I non-starburst to a Type II non-starburst, which under the right conditions, can undergo a starburst that will eventually

evolve back into a Type II non-starburst. This picture would naturally explain why a *one-to-one* correlation is not seen between bars and powerful central starbursts although in a statistical sense relatively luminous starbursts tend to be preferentially barred compared to normal galaxies (Hunt & Malkan 1999). Over its lifetime, a disk galaxy can undergo numerous episodes of bar-driven gas inflow characterized by these phases and gradually build up its central mass concentration and bulge, provided an adequate gas supply is maintained inside the corotation radius of the bar. This can be achieved by accreting gas-rich satellites in a barred disk galaxy or/and by externally inducing a new bar whose corotation radius encloses pre-existing gas reservoirs at large radii. Minor (1:10) to moderate (1:4) mass-ratio tidal interactions and mergers provide a natural way of doing both (Fig. 11) and are believed to be frequent over the last 8 Gyrs since  $z=1$  (Jogee et al. 2003; Mobasher et al. 2004).

## 12. INDIVIDUAL GALAXIES

The molecular gas distribution and kinematics of individual starbursts and non-starbursts are described below. Figures 14a–j and 15a–f show the total intensity (moment 0) and intensity-weighted velocity (moment 1) maps. For selected cases, p-v plots are shown if they can better represent complex kinematics.

### 12.1. *The Starbursts*

**NGC 4102, NGC 4536, NGC 3504, and NGC 470:** Within the inner kpc radius of the starbursts NGC 470, NGC 4102, NGC 3504, and NGC 4536, the molecular gas distribution (Figs. 14a–h) observed in *the sky plane* looks relatively symmetric about the line of nodes and is elongated along that position angle with an aspect ratio consistent with projection effects caused by the inclination of the galaxies. This implies that within the galactic plane of these four starbursts, most of the circumnuclear molecular gas has a relatively axisymmetric distribution of 300–600 pc radius. The moment 1 isovelocity contours (Figs. 14a–h) in the the inner 500 pc radius trace the characteristic spider diagram, suggesting the gas motions are predominantly circular. Several starbursts (NGC 4102, NGC 4536) show faint gas streams which extend from the relatively axisymmetric gas concentrations and curve along the leading edges of the large-scale stellar bar, connecting to the large-scale dust lanes. The gas streams show non-circular motions and are likely inflowing along the bar into the inner kpc region.

**NGC 2782 :** The starburst galaxy NGC 2782 differs in several respects from the other starbursts. The CO morphology in the sky plane is non-axisymmetric, double peaked and bar-like in the inner kpc radius (Fig. 14i–j). Since the galaxy has a low inclination of  $\sim 30$  deg, this elongated morphology is not due to projection effects, but reflects the intrinsic gas distribution in the galactic plane. Jogee et al. (1999) have presented evidence that the CO properties are consistent with the molecular gas responding to a nuclear stellar bar of radius  $\sim 1.3$  kpc, identified via isophotal fits to NIR images. The CO bar-like feature in NGC 2782 is offset in a leading sense with respect to the nuclear stellar bar and shows some non-circular kinematics (Jogee et al. 1999). The nuclear stellar bar appears to be

fueling gas from the CO lobes located a kpc radius down into the central 200 pc radius, where a powerful central starburst is forming stars at a rate  $\geq 3 M_{\odot} \text{ yr}^{-1}$  (Jogee et al. 1998). It is striking that NGC 2782 is the only starburst in our sample where *HST* images show the SF peaking at the center. In contrast, the other starbursts do not show evidence for strong nuclear stellar bars and their *HST* images show that SF does not extend into the inner 100 pc region.

### 12.2. *The Non-Starbursts*

**NGC 6951:** In NGC 6951, there are two CO peaks at a radius of  $6''$  (550 pc) lying nearly perpendicular to the large-scale stellar bar whose P.A. is 85 deg (Fig. 3b or 10a). Fainter emission around the peaks form two spiral-shaped streams which extend out and curve along the dust lanes on the leading edge of the large-scale bar. The molecular gas at the CO peaks and in the spiral streams shows complex non-circular motions (Figs. 15a–b). In NGC 6951, NGC 3351, and NGC 4314, the CO peaks lie near the OILR of the large-scale stellar bar (§ 10).

**NGC 3351:** In NGC 3351, the CO emission shows two peaks at a radius of  $\sim 7''$  (350 pc). As in NGC 6951, the two CO peaks lie nearly perpendicular to the large-scale stellar bar whose P.A. is 110 deg (Fig. 3b). The CO emission around the peaks appears to connect to the dust lanes which lie on the leading edge of the bar. The isovelocity contours curve near the CO peaks, suggesting non-circular streaming motions (Fig. 15c–d). Interior to the CO peaks, the p-v plot along the kinematic minor axis, where we are sensitive to the radial in-plane motion and vertical out-of-plane motion, shows complex non-circular kinematics.

**NGC 4314:** In NGC 4314, most of the gas is concentrated in a multiple-peaked relatively circular ring of radius  $5''$ – $7''$  (240 and 400 pc). Two faint CO spurs extend from the ring and intersect the dust lanes which lie on the leading edge of the large-scale stellar bar whose P.A. is 143 deg (Fig. 3b). Non-circular motions of 10 to 65  $\text{km s}^{-1}$  are detected in the CO spurs (Fig. 15e–f). The CO peaks lie near the OILR of the large-scale stellar bar (§ 10). Furthermore, inside the clumpy CO ring, ground-based (Friedli et al. 1996) and *HST* images of NGC 4314 reveal a nuclear stellar bar of radius  $4''$  (200 pc) at a position angle of -3 to -12 deg. In contrast to NGC 2782, the CO emission in NGC 4314 is not primarily concentrated along the nuclear stellar bar, but instead forms a clumpy ring at the end of the nuclear bar. The reason for such different gas and SF distributions in the two nuclear bars may be evolutionary in nature. In the case of NGC 4314, we may be seeing gas which is outside the corotation of a nuclear bar that formed earlier (Friedli & Martinet 1993). Conversely, in NGC 2782 we may be witnessing the early decoupling phase of a nuclear stellar bar induced by gas inside the OILR of the large-scale bar.

**NGC 4569:** NGC 4569 (Figs. 6a–d) differs from the above three non-starbursts in that it has a highly extended molecular gas distribution with complex kinematics and large linewidths of  $\sim 150 \text{ km s}^{-1}$ . A large fraction of the gas lies outside the inner kpc radius, extends out to a radius of  $20''$  (1.7 kpc), at a similar position angle as the large-scale stellar bar (Figs. 6a–b). This gas has

highly non-circular kinematics, as shown in the p-v plots along the kinematic major and minor axes (Figs. 6c-d). Along the kinematic major axis, velocities are generally positive (i.e., above the systemic value of  $-235 \text{ km s}^{-1}$ ) on the northeastern side, and negative on the southwest side. However, at a radius of  $5''$  (400 pc), near the feature marked ‘N1’ in Fig. 6c, the velocities change from  $+100 \text{ km s}^{-1}$  to a forbidden velocity of  $-75 \text{ km s}^{-1}$ . This indicates the presence of non-circular motions caused by in-plane azimuthal streaming motions or/and vertical motions out of the plane. As discussed in § 3, the CO properties of NGC 4569 are consistent with the early phases of bar-driven/tidally-driven gas inflow.

**NGC 3359:** In NGC 3359, the interferometric observations captured less than 30 % of the single dish flux, in contrast to the other sample galaxies (Table 5). The moment 0 map of NGC 3359 in Fig. 4b shows a very patchy CO distribution made up of a few clumps which lie away from the center. The present observations indicate that there is no bright centrally peaked CO distribution in the inner 500 pc of NGC 3359. The missing single dish flux may come from extended gas and/or diffuse low surface brightness CO in the central regions. As discussed in § 3, several authors have proposed that the large-scale stellar bar in NGC 3359 is young and may have been tidally triggered and it is possible that there are significant amounts of gas further out along the bar. To resolve this issue, future interferometric observations of a larger field of view, using a more compact array configuration needs to be carried out.

### 13. SUMMARY AND CONCLUSIONS

There is compelling observational and theoretical evidence that bars efficiently redistribute angular momentum in galaxies and drive gas inflows into the circumnuclear (inner 1–2 kpc) region. However, only few high resolution studies, based on a large sample of galaxies, have been carried out on the fate of gas in this region. In this study, we characterize the molecular environment, the onset of starbursts, and the secular evolution in the circumnuclear region of barred galaxies. We use a sample of local ( $D < 40 \text{ Mpc}$ ) barred non-starbursts and starbursts having high resolution ( $\sim 200 \text{ pc}$ ) CO ( $J=1 \rightarrow 0$ ), optical, NIR, H $\alpha$ , RC, Br $\gamma$ , and archival *HST* observations. Our results are summarized below.

(1) The circumnuclear regions of barred galaxies host  $3 \times 10^8$  to  $2 \times 10^9 M_{\odot}$  of molecular gas and have developed a molecular environment that *differs markedly* from that in the outer disk of galaxies. It includes molecular gas surface densities of  $500\text{--}3500 M_{\odot} \text{ pc}^{-2}$ , gas mass fractions of 10 to 30 %, epicyclic frequencies of several 100 to several  $1000 \text{ km s}^{-1} \text{ kpc}^{-1}$ , and velocity dispersions of 10 to  $40 \text{ km s}^{-1}$ . In this environment, gravitational instabilities set in only at very high gas densities (few  $100\text{--}1000 M_{\odot} \text{ pc}^{-2}$ ), but once triggered, they grow rapidly on a timescale of a few Myrs. This high density, short timescale, ‘burst’ mode may explain why the most intense starbursts tend to be in the central parts of galaxies. Furthermore, the high pressure, high turbulence ISM can lead to the formation of clouds with high internal dispersion and mass, and hence may favor the formation of massive clusters as suggested by Elmegreen et al (1993). The molecular environment in

the inner kpc of the ULIRG galaxy Arp 220 is a scaled-up version of the one in these barred galaxies, suggesting that interactions build up even more extreme conditions.

(2) We suggest that the wide variety in CO morphologies is due to different stages of bar-driven inflow. A non-starburst like NGC 4569 which is in the *early* stages of bar-driven inflow has a highly extended molecular gas distribution where a large fraction of the circumnuclear gas is still along the large-scale stellar bar, outside the outer inner Lindblad resonance (OILR). This gas shows large non-circular kinematics and is not forming stars efficiently. Several other galaxies studied by others such as NGC 7479 (Laine et al. 1999), NGC 7723 (Chevalier & Furenlid 1978), NGC 1300, and NGC 5383 (Tubbs 1982) may be in a similar phase. In contrast, we present dynamical and morphological that the other non-starbursts and starbursts are in *later* stages of bar-driven inflow. Most of their circumnuclear gas is inside or near the OILR of the bar and has predominantly circular motions. Across the sample, we estimate upper limits in the range  $43$  to  $115 \text{ km s}^{-1} \text{ kpc}^{-1}$  for the bar pattern speed and an OILR radius of  $> 500 \text{ pc}$ .

(3) The barred starbursts and non-starbursts have circumnuclear SFRs of 3 to 11 and  $0.1\text{--}2 M_{\odot} \text{ yr}^{-1}$ , respectively. For a given amount of molecular hydrogen ( $M_{\text{H}_2}$ ) in the inner 1–2 kpc (assuming a standard CO-to- $\text{H}_2$  conversion factor), barred galaxies can show an order of magnitude variation in the SFR/ $M_{\text{H}_2}$  over this region. This range seems related to the fact that the gas surface densities in the starbursts are larger ( $1000\text{--}3500 M_{\odot} \text{ pc}^{-2}$ ) and close to the Toomre critical density over a large region. The Toomre  $Q$  parameter reaches its minimum value of  $\sim 1\text{--}2$  in the region of star formation, despite an order of magnitude variation in the gas surface density and epicyclic frequency. This suggests that the onset of gravitational instabilities, as characterized by  $Q$ , plays an important role even in the inner kpc region.

(4) The dynamical mass enclosed within the inner kpc radius of the barred galaxies in our sample is  $6\text{--}30 \times 10^9 M_{\odot}$ . Molecular gas makes up 10%–30% of the dynamical mass and in the circumnuclear starbursts, it is fueling a SFR of  $3\text{--}11 M_{\odot} \text{ yr}^{-1}$  in the inner kpc. As these starbursts use up their gas and evolve into the post-starburst phase, they will build young, massive, high  $V/\sigma$  stellar components within the inner kpc, inside the OILR of the large-scale bar. *Such compact stellar components will likely belong to the class of pseudo-bulges* (Kormendy 1993) whose light distribution and kinematics are more consistent with a disk than with a spheroidal bulge component. We present evidence of such a component in NGC 3351, which seems to be in a post-burst phase. The observations are consistent with the idea that over a galaxy’s lifetime, it can experience numerous episodes of bar/tidally driven gas inflows, which lead to a gradual buildup of its central mass concentration, the formation of pseudo-bulges, and perhaps even secular evolution along the Hubble sequence.

### 14. ACKNOWLEDGMENTS

Support for this work was generously provided by NSF grant AST 99-81546, and a grant from the K. T. and E. L. Norris Foundation. SJ also acknowledges support from the National Aeronautics and Space Administration (NASA)

under LTSA Grant NAG5-13063 issued through the Office of Space Science, a Grant-in-Aid of Research from Sigma Xi (The Scientific Research Society), an AAUWEF Fel-

lowship, and a Zonta International Amelia Earhart Fellowship.

## REFERENCES

- Aalto, S., et al. 1994, *A&A*, 286, 365  
 Aalto, S., et al. 1995, *A&A* 300, 369.  
 Athanassoula, E. 1992, *MNRAS*, 259, 345  
 Baker, A. J. 2000, Ph.D. thesis  
 Ball, R. 1986, *ApJ*, 307, 453  
 Benedict, G. F., Smith, B. J., and Kenney, J. D. P., 1996, *AJ*, 111, 1861  
 Berentzen, I., Shlosman, I., & Jogee, S. 2005, *ApJ*, submitted (astro-ph/0501352)  
 Binney, J., & Tremaine, S. 1987, *Galactic Dynamics*, ed. Ostriker, J. P. (Princeton, N. J.: Princeton University Press)  
 Bloemen, J. B. G. M., et al. 1986, *A&A*, 154, 25  
 Byrd, G., et al. 1994, *AJ*, 108, 476  
 Cayatte, V., van Gorkom, J. H., Balkowski, C. & van Gorkom, J. H. 1994 *AJ*, 107, 1003  
 Chevalier, R. A., & Furenlid, I. 1978, *ApJ*, 225, 67  
 Combes, F., & Gerin, M. 1985, *A&A*, 150, 327  
 Combes, F., Debasch, F., Friedli, D., & Pfenniger, D. 1990, *A&A*, 233, 82  
 Condon, J. J., Condon, M. A., Gisler, G., Puschell, J. J. 1982, *ApJ*, 252, 102  
 Condon, J. J., Helou, G., Sanders, D. B., & Soifer, T. B. 1990, *ApJS*, 73, 359  
 Condon, J. J., & Yin, Q. F. 1990, *ApJ*, 357, 97  
 Condon, J. J. 1992, *ARAA*, 30, 575  
 Contopoulos, G. & Papayannopoulos, T. 1980, *A&A* 92, 33  
 Courteau, S., de Jong, R. S., Broeils, A. H. 1996, *ApJ* 457, L73.  
 Das, M. & Jog, C. J. 1995, *ApJ*, 451, 167  
 Debattista, V. P., & Sellwood, J. A. 2000, *ApJ*, 543, 704  
 de Vaucouleurs, G., de Vaucouleurs, A., Corwin Jr., H. G., Buta, R. J., Paturel, G., & Fouque, P. 1991, *Third Reference Catalogue of Bright Galaxies* (New York: Springer) (RC3)  
 Deharveng, J. M., et al. 1994, *A&A*, 289, 715  
 Devereux, N. A. 1989, *ApJ*, 346, 126  
 De Jong, R. S. 1996, *A&A* 313, 45  
 Dickey, J. M., Hanson, M. M., & Helou, G. 1990, *ApJ*, 352, 522  
 Dickman, R. L. 1975, *ApJ*, 202, 50  
 Dickman, R. L., Snell, R. L., & Schloerb, F. P. 1986, *ApJ*, 309, 326  
 Eder, J. A. 1990, Ph.D. thesis, Yale University  
 Elmegreen, B. G. 1989, *ApJ*, 338, 178  
 Elmegreen, B. G. 1990, *ApJ*, 357, 125  
 Elmegreen, B. G., Kaufman, M., & Thomasson, M. 1993, *ApJ*, 412, 90  
 Elmegreen, B. G. 1995, *MNRAS*, 275, 944  
 Elmegreen, D. M., Chromey, F. R., Santos, M., & Marshall, D. 1997, *AJ*, 114, 1850  
 Elmegreen, B. G., Elmegreen, D. M., & Hirst, A. C. 2004, *ApJ*, 612, 191  
 Friedli, D., & Martinet, L. 1993, *A&A*, 277, 27  
 Friedli, D. & Benz, W., & Kennicutt, R. 1994, *ApJ*, 430, L105  
 Friedli, D. & Benz, W. 1995, *A&A*, 268, 65  
 Friedli, D., et al. 1996, *A&AS*, 118, 461  
 Gammie, C. F., Ostriker, J. P., & Jog, C. J. 1991, *ApJ*, 378, 565  
 Goldreich, P., & Lynden-Bell, D. 1965a, *MNRAS*, 130, 125  
 Grosbøl, P. J. 1985, *A&AS*, 60, 261  
 Guiricin, G., Tamburni, L., Mardirossin, F., Mezzetti, M., & Monaco, P. 1994, *ApJ*, 427, 202  
 Handa, T., Sofue, Y., & Nakai, N. 1991, in *Proceeding of IAU Symposium 146, Dynamics of Galaxies and Their Molecular Cloud Distributions*, ed. F. Combes and F. Casoli (Dordrecht: Kluwer), 156  
 Heckman, T. M., Armus, L., & Miley, G. K. 1990, *ApJS*, 574, 833  
 Helfer, T. T., & Blitz, L. 1993, *ApJ*, 419, 86  
 Heller, C. H., & Shlosman, I. 1996  
 Hunt, L. K., & Malkan, M. A. 1999, *ApJ*, 516, 660  
 Jog, C. J., & Solomon, P. M. 1984, *ApJ*, 276, 127  
 Jog, C. J. 1992, *ApJ*, 390, 378  
 Jogee, S., & Kenney, J. D. P. 1996, in *ASP Conference Series*, Vol. 91, *Proceedings of IAU Colloquium 157, Barred Galaxies*, ed. R. Buta, D. A. Crocker, & B. G. Elmegreen (San Francisco: ASP), 230  
 Jogee, S., Kenney, J. D. P., & Smith, B. J. 1998, *ApJL*, 494, L185  
 Jogee, S., Kenney, J. D. P., & Smith, B. J. 1999, *ApJ*, 526, 665  
 Jogee, S. 1999, Ph.D. thesis, Yale University  
 Jogee, S. 2001, in *Proceedings of Rinberg Workshop, Starbursts Near and Far*, eds L. Tacconi & D. Lutz (Heidelberg: Springer-Verlag), 182 (astro-ph/0201202)  
 Jogee, S., Knapen, J. H., Laine, S., Shlosman, I., Scoville, N. Z., & Englmaier, P. 2002a, *ApJL*, 570, L55 (astro-ph/0201208)  
 Jogee, S., Shlosman, I., Laine, S., Knapen, J. H., Englmaier, P., Scoville, N. Z., & Wilson, C. D. 2002b, *ApJ*, xxxxxxxxx (astro-ph/0202270)  
 Jogee, S., & GEMS/GOODS collaboration 2003 *IAU Symposium* 216, *Maps of the Cosmos*.  
 Jogee, S., Barazza, F., Rix, H.-W., Shlosman, I. et al. 2004a, *ApJL*, 615, L105 [J04b];  
 Jogee, S., Barazza, F., Rix, H.-W., et al. 2004b, in *Penetrating Bars through Masks of Cosmic Dust: The Hubble Tuning Fork Strikes a New Note*, eds. D. L. Block, I. Puerari, K. C. Freeman, R. Groess, & E. K. Block (Dordrecht: Springer), *Astr. & Sp. Sc. Library*, 319, 291 (astro-ph/0408267)  
 Jogee, S., 2004, in *Lecture Notes in Physics: "AGN Physics on All Scales"*, Eds. D. Alloin, R. Johnson, & P. Lira (Springer: Berlin Heidelberg New York), Chapter 6, in press (astro-ph/0408383)  
 Kenney, J. D. P., & Young, J. S. 1989, *ApJ*, 344, 171  
 Kenney, J. D. P., & Lord, S. D. 1991, *ApJ*, 381, 118  
 Kenney, J. D. P., Wilson, C. D., Scoville, N. Z., Devereux, N. A., & Young, J. S. 1992, *ApJ*, 395, L79  
 Kenney, J. D. P., Carlstrom, J. E., & Young, J. S. 1993, *ApJ*, 418, 687  
 Kennicutt, R. C., Jr. 1983, *ApJ*, 272, 54  
 Kennicutt, R. C., Jr. 1989, *ApJ*, 344, 685  
 Kennicutt, R. C. 1998a, *ARAA*, 36, 189  
 Kennicutt, R. C., Jr., 1998b, *ApJ*, 498, 541  
 Kim, W., Ostriker, E. C., & Stone, J. M. 2002, *ApJ*, 581, 1080  
 Knapen, J. H., et al. 1995, *ApJ*, 454, 623  
 Kohno, K., Kawabe, R., & Vila-Vilar, B. 1999, *ApJ*, 511, 157  
 Kormendy, J. 1983, *ApJ*, 265, 632  
 Kormendy, J. 1993, in *Proceedings of IAU Symposium 153, Galactic bulges*, ed. H. DeJonghe and H. J. Habing, (Dordrecht: Kluwer), 209  
 Kormendy, J., & Kennicutt, R. C. 2004, *ARAA*, 42, 603  
 Kwan, J. 1979, *ApJ*, 229, 567  
 Laine, S., Kenney, J. D. P., Yun, M. S., & Gottesman, S. T. 1999, *ApJ*, 511, 709  
 Laine, S. & Heller, C. H. 1999, *MNRAS*, 308, 557  
 Larson, R. B. 1985, *MNRAS*, 214, 379  
 Martin P., & Roy, R. 1995, *ApJ*, 445, 161  
 Merritt, D., & Sellwood, J. A. 1994, *ApJ*, 425, 551  
 Mobasher, M., Jogee, S., Dahlen, T., de Mello, D., Lucas, R. A., Conselice, C. J., Grogin, N. A., & Livio M. 2004, *ApJL*, 600/2, 74 (astro-ph/0309066)  
 Munoz-Tunon, C., Vilchez, J. M., Castaneda, H. O., & Beckman, J. E. 1989, *Ap&SS*, 157, 165  
 Padin, S., Scott, S. L., Woody, D. P., Scoville, N. Z., Selsing, T. V., Finch, R. P., Giovanine, C. J., & Lawrence, R. P. 1991, *PASP*, 103, 461  
 Pfenniger, D. & Norman, C. 1993, *ApJ*, 409, 91  
 Piner, B., Glenn, S., James, M., & Teuben, P. J. 1995, *ApJ*, 449, 508  
 Puxley, P. J., Hawarden, T. G., & Mountain, C. M. 1988, *MNRAS*, 234, 29  
 Puxley, P. J., Hawarden, T. G., & Mountain, C. M. 1990, *ApJ*, 364, 77.  
 Quillen, A. C., Frogel, J. A., Kenney, J. D. P., Pogge, R. W., & DePoy, D. L. 1995, *ApJ*, 441, 549  
 Regan, M. W., Vogel, S. N., & Teuben, P. J. 1997, *ApJ*, 482, L143  
 Safronov, V. S. 1960, *Annales d'Astrophys*, 23, 979  
 Saikia, D. J., Pedlar, A., Unger, S. W., & Axon, D. J. 1994, *MNRAS*, 270, 46  
 Sakamoto, K., Scoville, N. Z., Yun, M. S., Crosas, M., Genzel, R. et al. 1999, *ApJ*, 514, 68  
 Sandage, A. & Bedke, J., 1994, *The Carnegie Atlas of Galaxies* (Washington D. C.: Carnegie Institute of Washington)  
 Scoville, N. Z., Sanders, D. B., & Clemens, D. P. 1986, *ApJ*, 310, L7  
 Scoville, N. Z., et al. 1987, *ApJS*, 63, 821  
 Scoville, N. Z., & Sanders, D. B. 1987, in *Interstellar Processes*, ed. D. J. Hollenbach and H. A. Thronson (Dordrecht: Reidel), 21  
 Scoville, N. Z., et al. 1993, *PASP*, 105, 1982  
 Scoville, N. Z., Yun, M.S., & Bryant, P.M. 1997, *ApJ*, 484, 702  
 Sellwood, J. A. 1993, in *Proceedings of IAU Symposium 153, Galactic bulges*, ed. H. DeJonghe and H. J. Habing, (Dordrecht: Kluwer), 391  
 Shlosman, I., Frank, J., and Begelman, M. C. 1989, *Nature*, 338, 45  
 Smith, B. J. 1994, *AJ*, 107, 1695

Strong, A. W., et al. 1988, A&A, 207, 1  
Tacconi, L. J., & Young, J. S. 1986, ApJ, 308, 600  
Taylor, C. L., et al. 1994, AJ, 107, 971  
Toomre, A. 1964, ApJ, 139, 1217

Tubbs, A. D. 1982, ApJ, 255, 458  
Vila-Costas, M. B., & Edmunds, M. G. 1992, MNRAS, 259, 121  
Wall, W. F., & Jaffe, D. T. 1990, ApJ, 361, L45  
Young, J. S., et al. 1995, ApJS, 98, 219

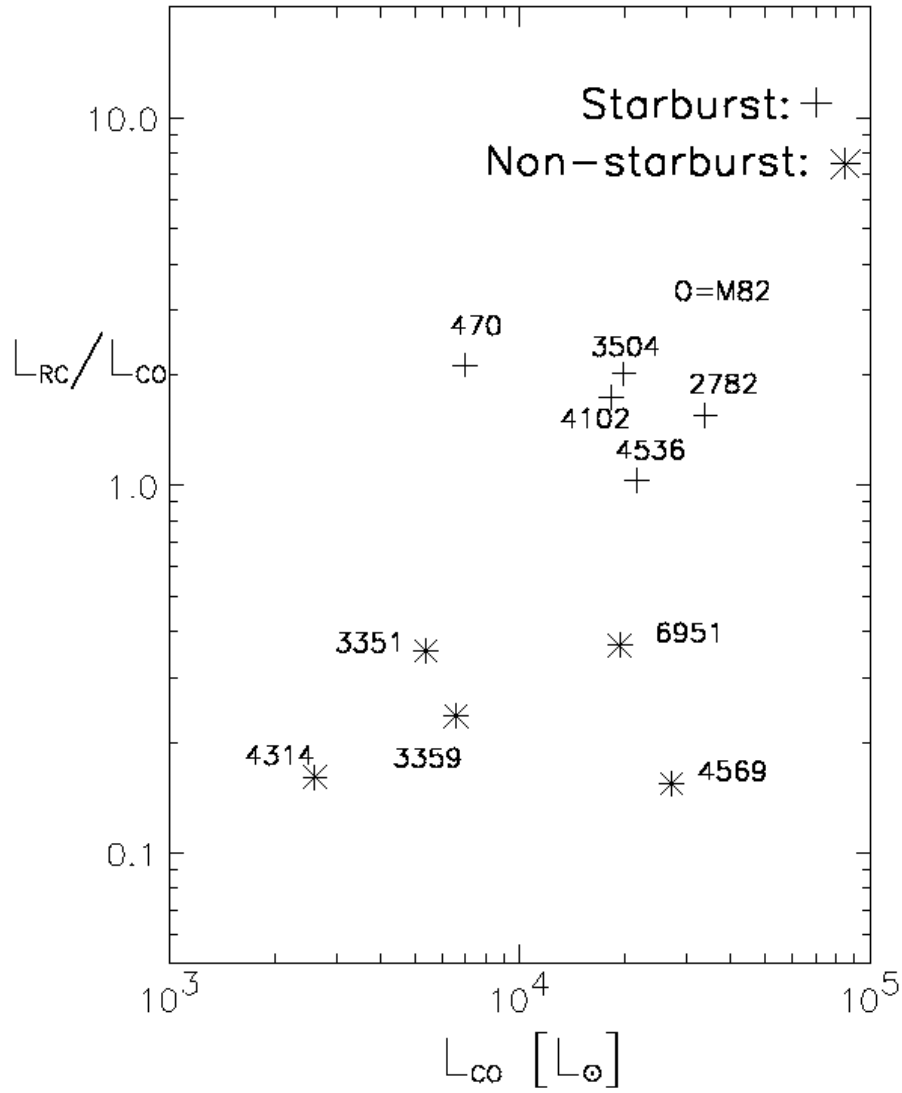


**Fig. 1— The sample of barred starbursts and non-starbursts:**  $L_{RC}$  is the RC luminosity at 1.49 GHz and  $L_{CO}$  is the single dish CO luminosity. Both are measured in the central  $45''$  diameter or inner 1-2 kpc radius. The galaxies in our sample (designated by their NGC numbers) as well as the prototypical starburst M82 are plotted. Note that for a given  $L_{CO}$ , the star formation rate per unit mass of molecular hydrogen as characterized by  $L_{RC}/L_{CO}$  can vary by an order of magnitude.

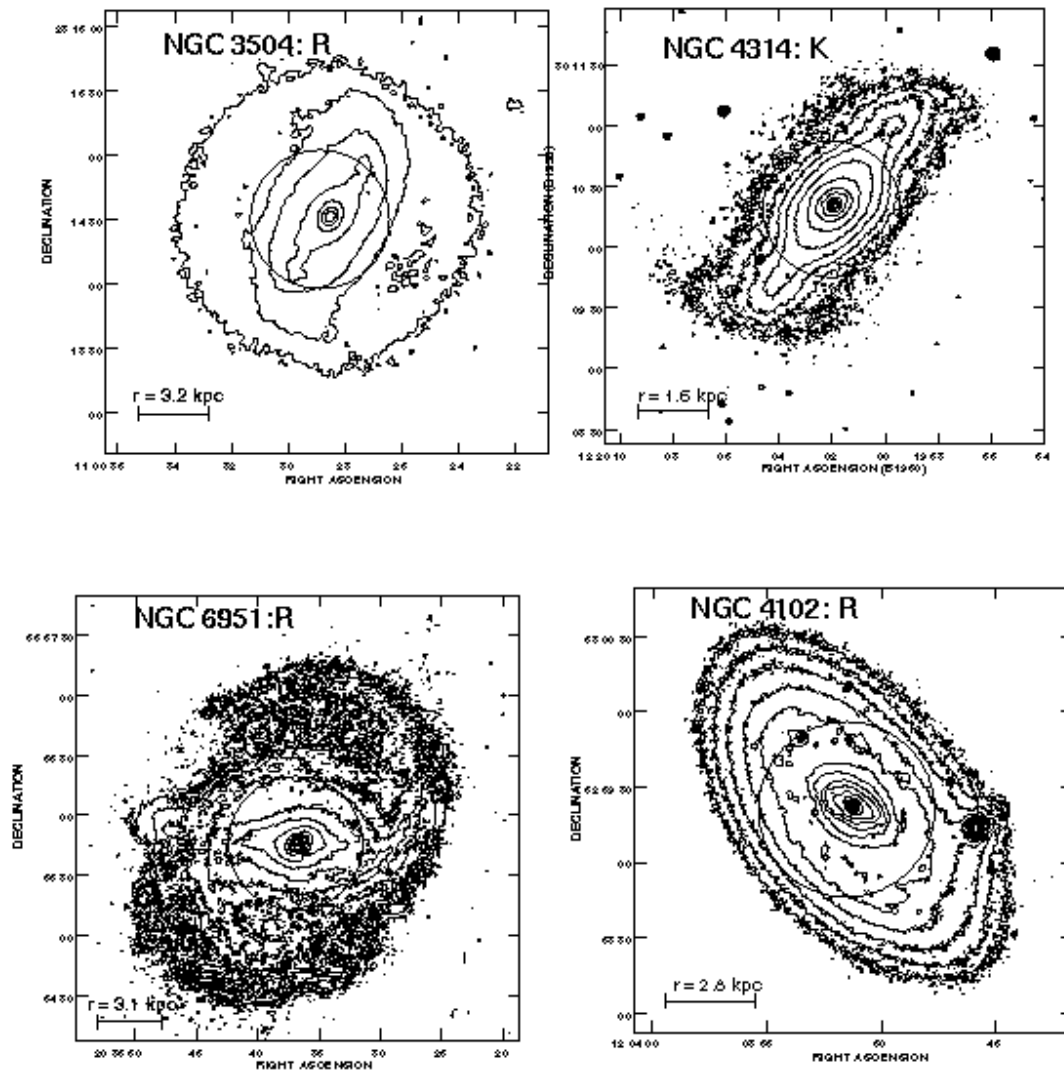


**Fig. 2— Evidence for large-scale stellar bars/oval distortions:** (a) *R*-band image of NGC 3504 (b) *K*-band image of NGC 4314, (c) *R*-band image of NGC 6951, and (d) the *R*-band image of NGC 4102. These images illustrate the large-scale stellar bars and oval distortions in typical sample galaxies. The dotted circle shows the OVRO CO(1–0) half power beam width (65'') at 115 GHz and illustrates the region where molecular gas is mapped.

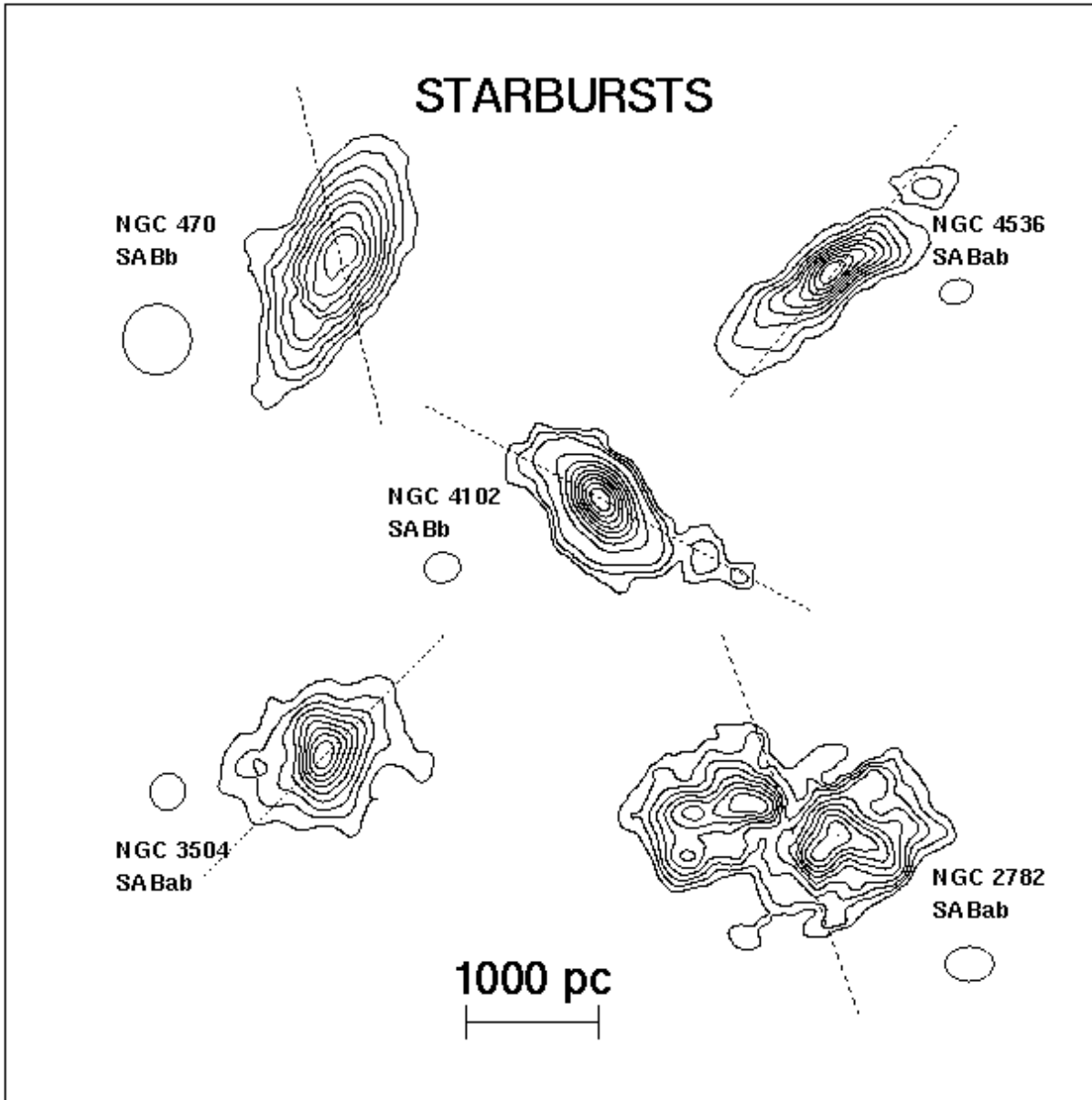


**Fig. 3a— The circumnuclear molecular gas morphology:** The CO total intensity (moment 0) maps of barred starbursts and non-starbursts are shown. The size of the synthesized beam is shown next to each map. The dotted line shows the position angle of the large-scale stellar bar/oval. The contour levels plotted are specified in Table 10. There is a wide variety of circumnuclear CO morphologies including relatively axisymmetric annuli or disks (starbursts NGC 4102, NGC 3504, NGC 4536, and non-starbursts NGC 4314), elongated double-peaked and spiral morphologies (starburst NGC 2782 and non-starbursts NGC 3351 and NGC 6951), and extended distributions elongated along the bar (non-starburst NGC 4569). The relationship between the gas distribution and the resonances of the bar is discussed in § 10 and Fig. 9.

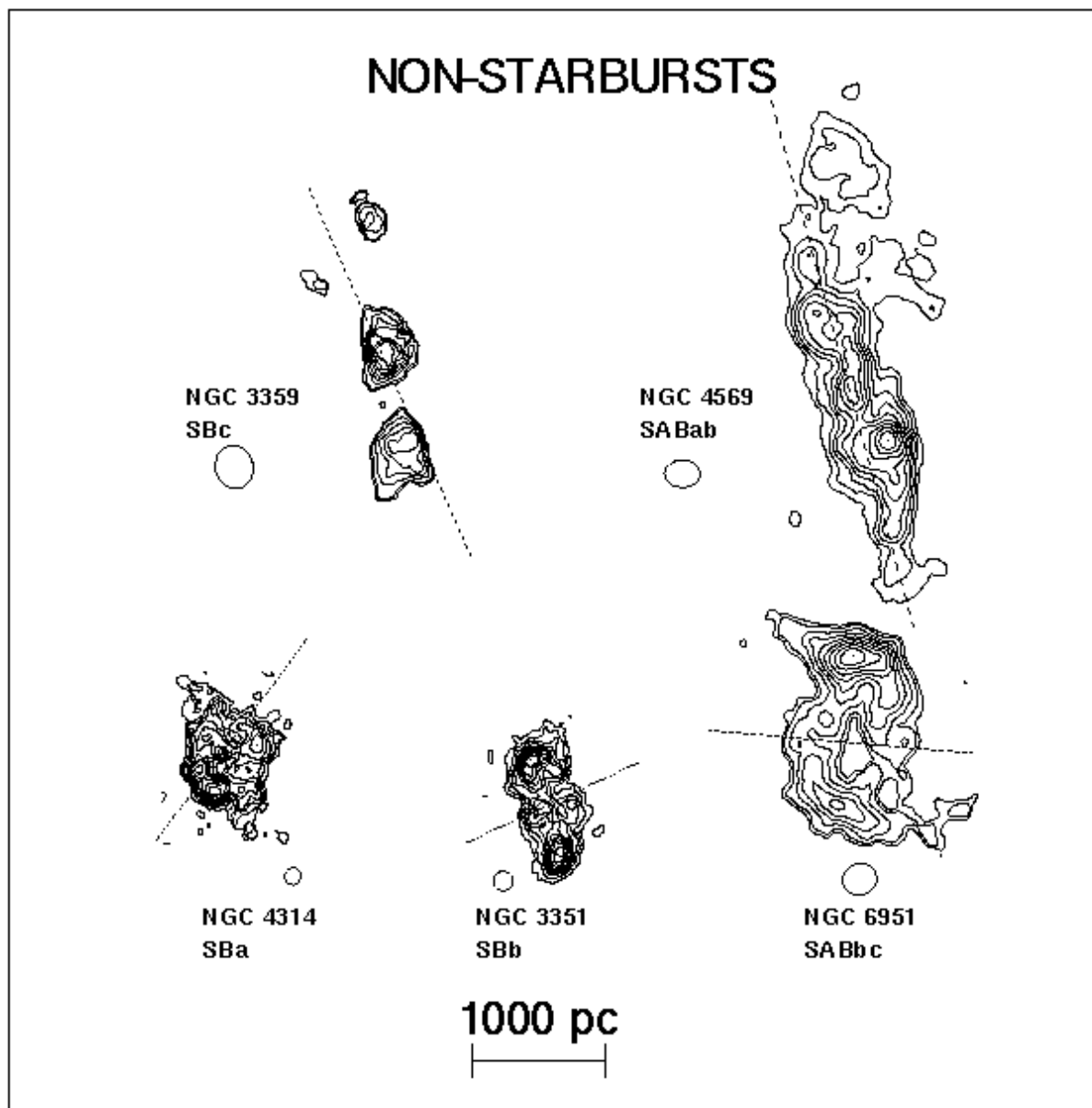
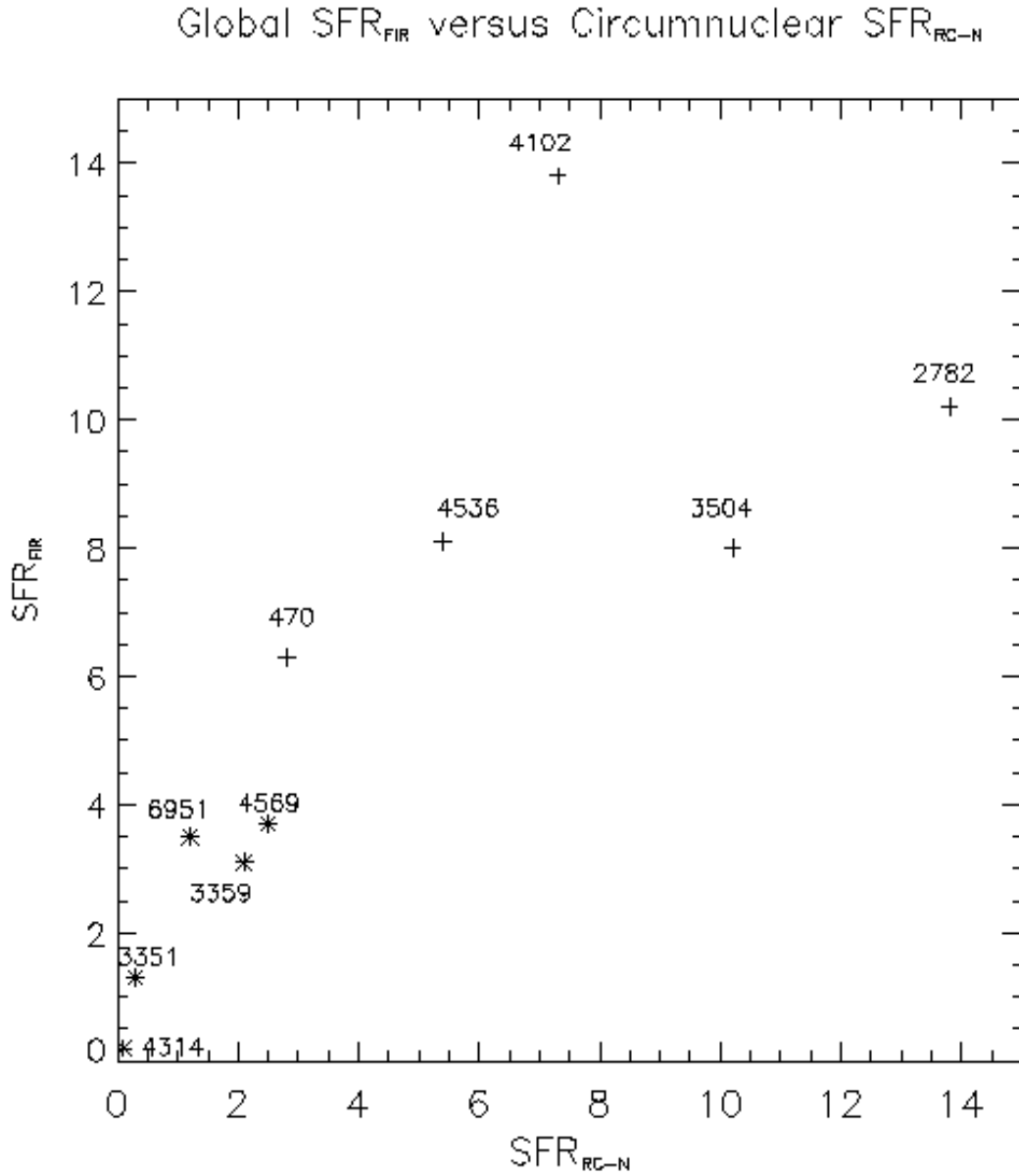
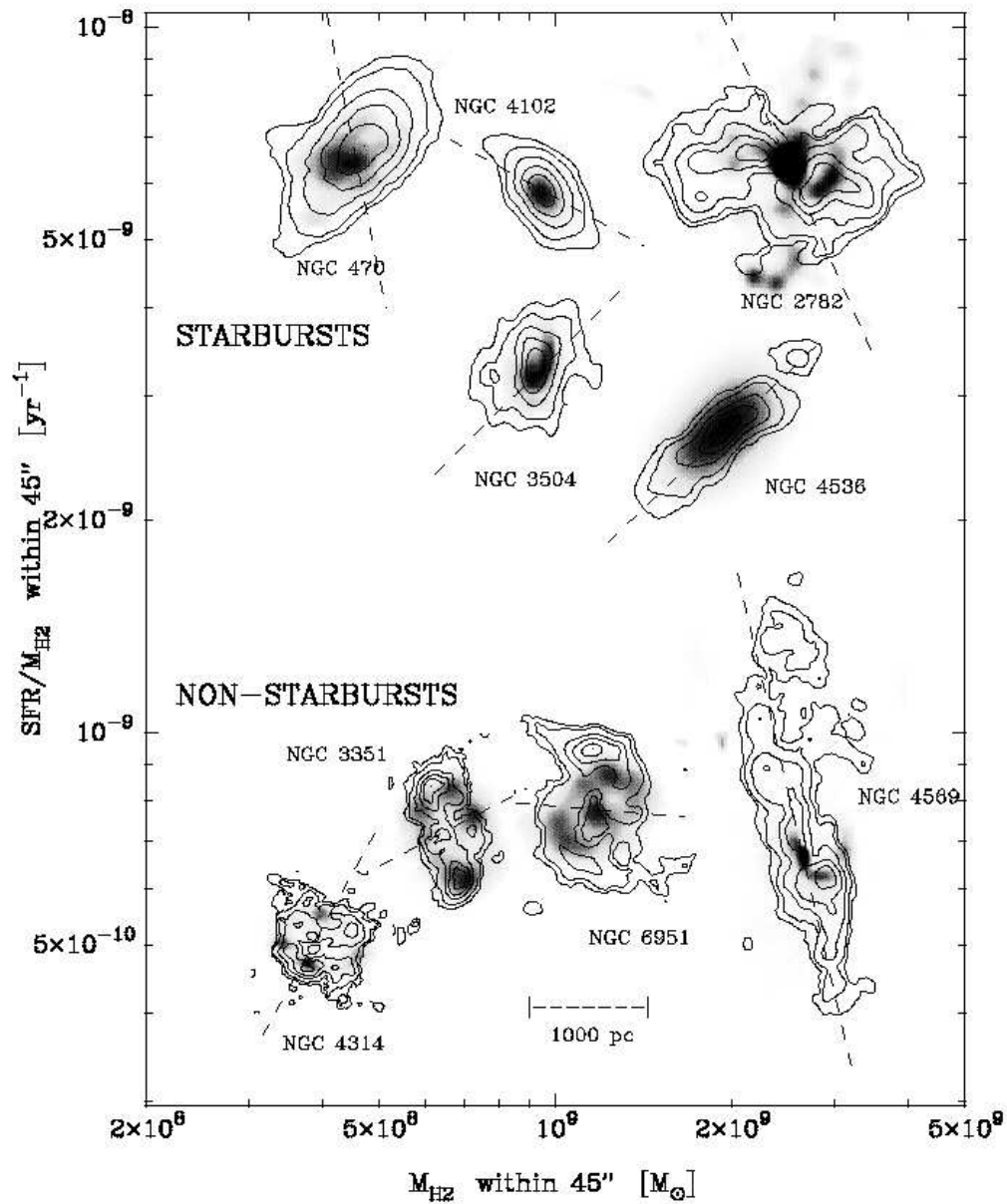


Fig. 3b— The circumnuclear molecular gas morphology: As in 3a, but showing the barred non-starbursts.



**Fig. 4— A comparison of the SFRs estimated from different tracers:** The star formation rate ( $SFR_{\text{RC-N}}$ ) estimated from the non-thermal RC in 45'' is plotted against the star formation rate ( $SFR_{\text{FIR}}$ ) estimated from the total FIR luminosity.  $SFR_{\text{RC-N}}$  is less than  $SFR_{\text{FIR}}$  as expected, except in NGC 2782 and NGC 3504, where  $SFR_{\text{RC-N}}$  is 10 to 30 % higher.



**Fig. 5— Distribution of molecular gas and SF in the barred starbursts and non-starbursts:** In the  $\text{SFR}/M_{\text{H}_2}$  versus  $M_{\text{H}_2}$  plane, the CO intensity (contours) is overlaid on the 1.5 or 4.9 GHz radio continuum map (greyscale) of NGC 4102, NGC 2782, and NGC 6951 and on the  $\text{H}\alpha$  map for the other galaxies. The greyscale traces the star formation activity and in the case of NGC 6951, it also shows the Seyfert 2 nucleus in the inner 100 pc. The  $\text{H}\alpha$  and RC maps have a resolution of  $1.0 - 1.5''$ . The synthesized CO beam is typically  $2''$  or 100–200 pc. The dotted line is the P.A. of the large-scale stellar bar/oval. The contour levels plotted are specified in Table 10.

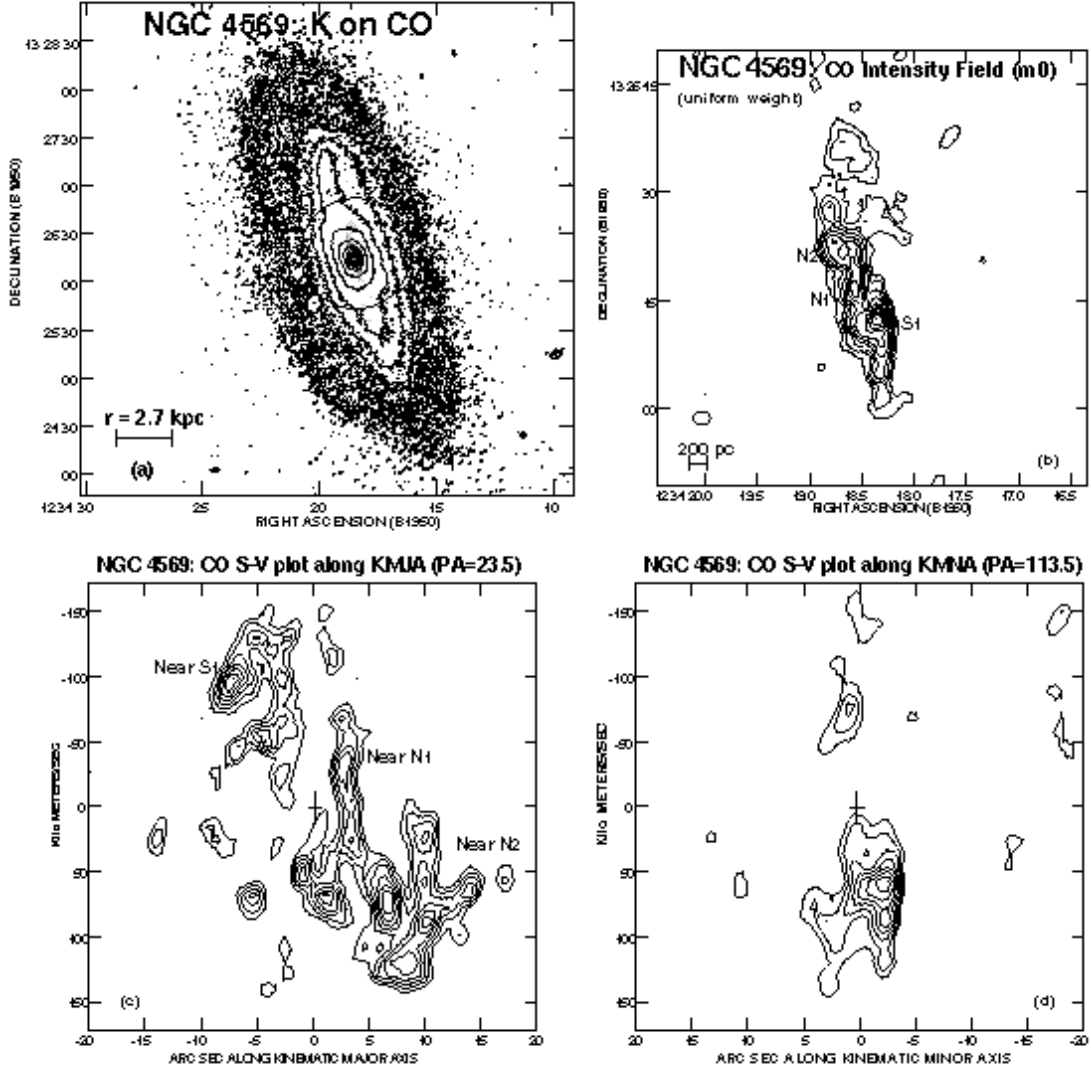


**Fig. 6— Gas distribution and kinematics in NGC 4569:** (a) The  $K$ -band image (contours) with a field of view of  $5'$  ( $25.9$  kpc) shows an asymmetric stellar bar. The overlaid circle shows the  $65''$  half power beam width of the CO interferometric observations. The CO distribution inside the beam is shown in greyscale. (b) The uniformly weighted ( $2.65'' \times 2.01''$  or  $223 \times 169$  pc) CO total intensity map in the central  $6''$  ( $5.0$  kpc) shows an extended molecular gas distribution in NGC 4569. Contour levels plotted are  $3.20 \text{ Jy beam}^{-1} \text{ km s}^{-1} \times (1, 2, 3, 4, 5, 6, 7, 8, 9, 10)$ . The gas extends out to a large ( $20''$  or  $1.7$  kpc) radius, and is elongated along the direction of the large-scale stellar bar. (c), (d) show the p-v plots along the kinematic major and minor axes. The molecular gas extends out to a  $2$  kpc radius and shows very disturbed kinematics. Along the kinematic major axis, velocities are generally positive (i.e. above the systemic value) on the northeastern side. However, at a radius of  $5''$  ( $400$  pc), near the feature marked 'N1' in (b), the velocities change from  $\sim +100 \text{ km s}^{-1}$  to a forbidden velocity of  $-75 \text{ km s}^{-1}$ .

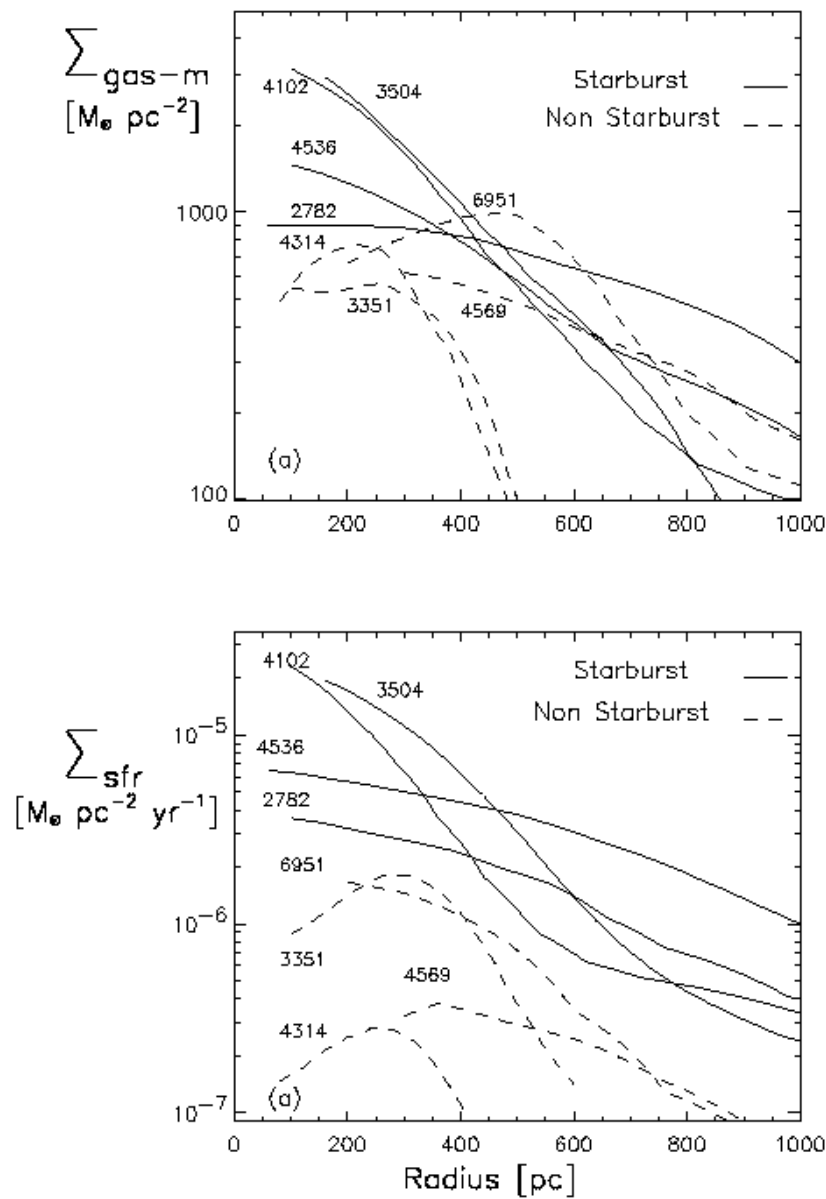


**Fig. 7**— (a), (b) show the azimuthally averaged molecular gas surface density ( $\Sigma_{\text{gas}}$ ) and the SFR per unit area ( $\Sigma_{\text{SFR}}$ ). The extinction-corrected profiles are convolved to a similar resolution of 100-200 pc for all the galaxies. Quantities are plotted starting at a radius  $\geq$  half the size of the synthesized beam (typically  $2''$  or 150 pc). Most of the starbursts have developed larger molecular gas surface densities (1000-3500  $M_{\odot} \text{pc}^{-2}$ ) in the inner 500 pc radius than the non-starbursts, for a given CO-to- $\text{H}_2$  conversion factor. In the inner 500 pc radius of the starbursts, both  $\Sigma_{\text{gas-m}}$  and  $\Sigma_{\text{SFR}}$  increase toward the center.

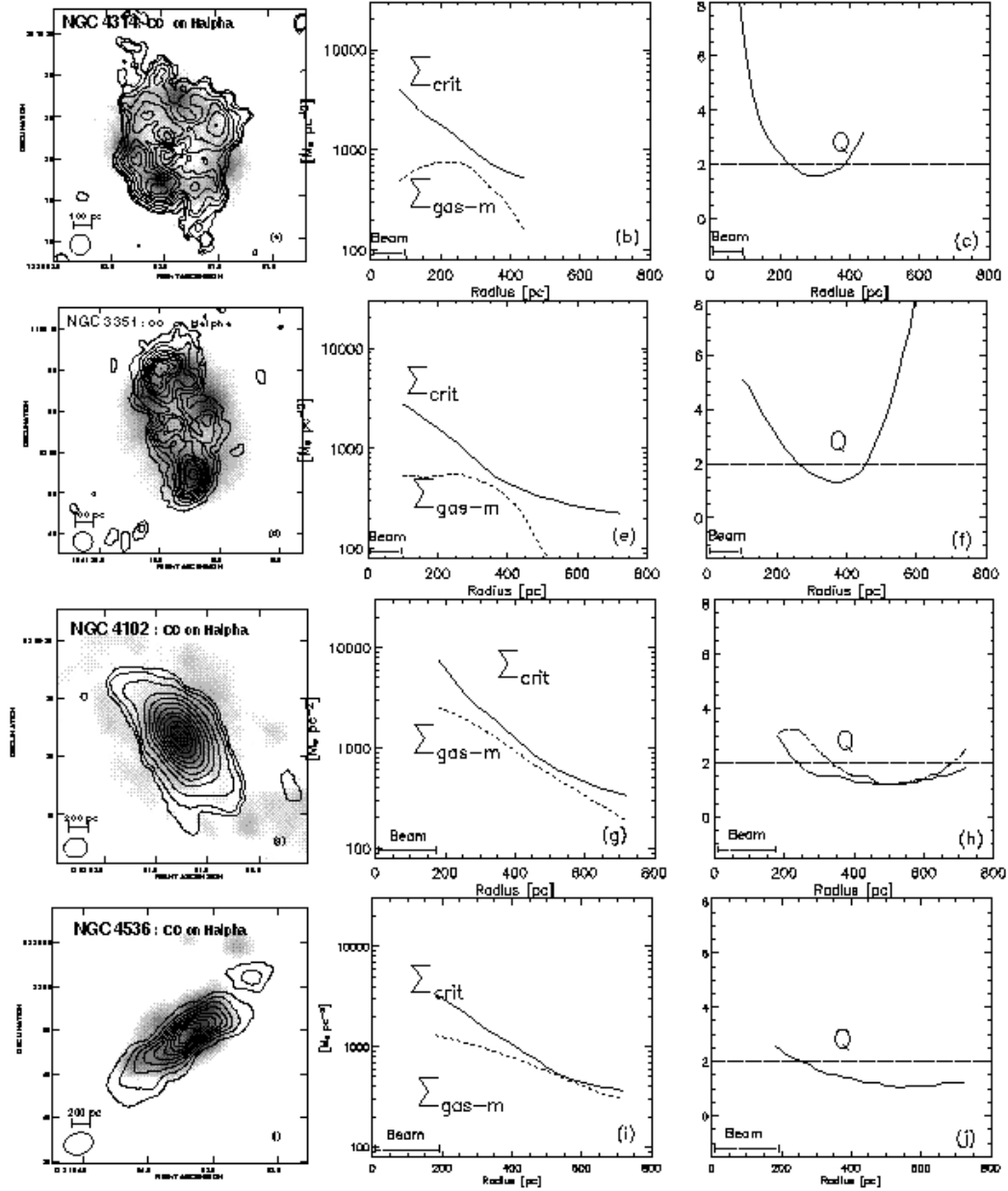


**Fig. 8— Comparison of the gas density with the Toomre critical density in the non-starbursts and starbursts:** **Column 1:** The CO distribution (contours) on the H $\alpha$  (greyscale) for the non-starbursts NGC 4314 and NGC 3351, and the starbursts NGC 4102 and NGC 4536. **Column 2:** The molecular gas surface density  $\Sigma_{\text{gas-m}}$  and the critical density ( $\Sigma_{\text{crit}} = \alpha \kappa \sigma / \pi G$ ) for the onset of gravitational instabilities assuming  $\alpha = 1$ . Quantities are plotted starting at a radius equal to the CO beam size ( $\sim 2''$ ). **Column 3:** The Toomre  $Q$  parameter ( $\Sigma_{\text{crit}}/\Sigma_{\text{gas}}$ ). The horizontal line denotes the value of  $Q$  in the outer disk of spirals where Kennicutt (1989) finds  $\alpha = 0.7$ . In the non-starbursts NGC 4314 and NGC 3351, HII regions are concentrated in a gas-rich annulus of radius 350 pc ( $7''$ ) while further in, the star formation activity drops sharply despite large gas surface densities above  $400 M_{\odot} \text{ pc}^{-2}$ . In these non-starbursts,  $Q$  reaches its lowest value (1–2) in the ring of HII regions while at lower radii  $Q$  increases to  $\sim 6$ , suggesting sub-critical gas densities. In the starbursts NGC 4102 and NGC 4536,  $Q$  remains remarkably close to 1–2 over a wide region, between a radius of 250 to 700 pc, although the gas surface density and the epicyclic frequency both vary by nearly an order of magnitude.

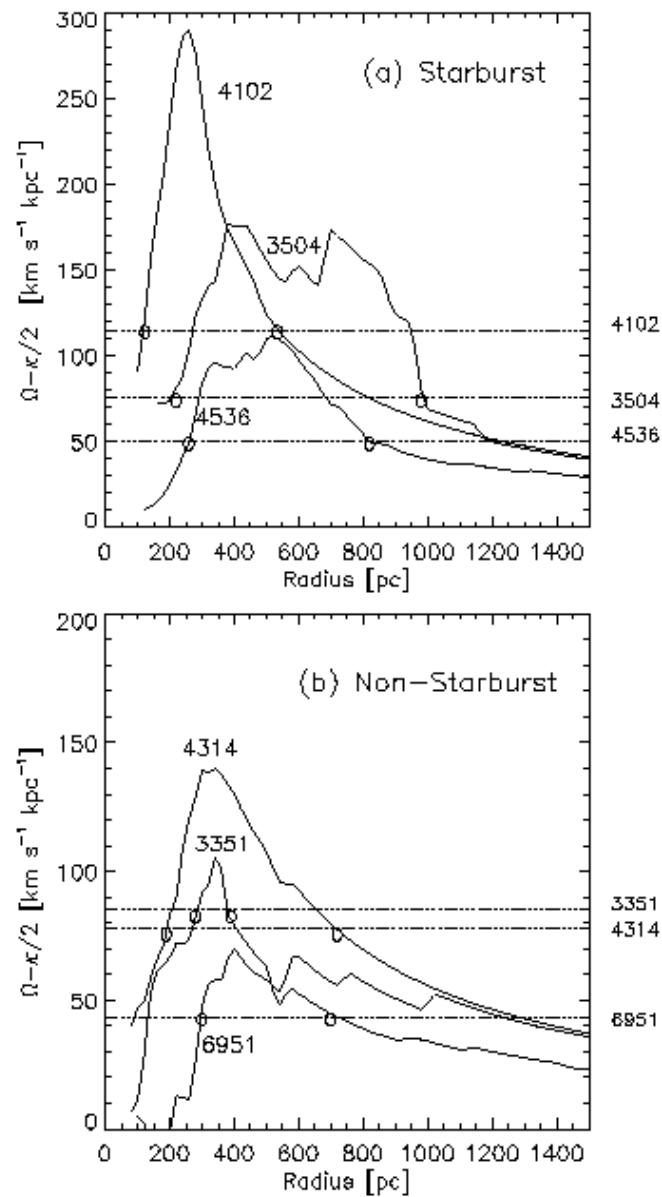


**Fig. 9— Inner Lindblad resonances in the barred starbursts and non-starbursts:**  $[\Omega - \kappa/2]$  is plotted against radius for select (a) starbursts and (b) non-starbursts. The bar pattern speed  $\Omega_p$  is drawn as horizontal lines and estimated by assuming that the corotation resonance is near the end of the large-scale stellar bar (see Table 9). Under the epicycle theory for a weak bar, the intersection of  $[\Omega - \kappa/2]$  with  $\Omega_p$  defines the locations of the ILRs. In these systems, the circumnuclear gas is concentrated inside the outer ILR of the large-scale stellar bar/oval.

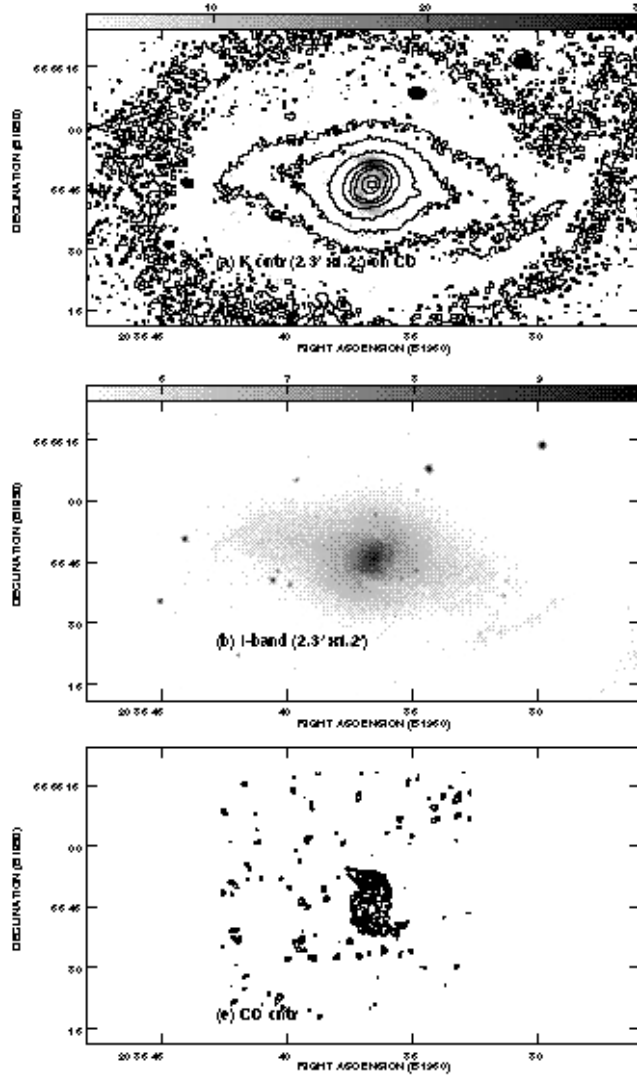


**Fig. 10— Relationship between the large-scale stellar bar, large-scale dust lanes, and circumnuclear CO morphology in NGC 6951:** (a) The *K*-band image (contours) of NGC 6951 with a  $2.3' \times 1.2'$  ( $12.7 \times 6.9$  kpc) field of view shows the inner region of the large-scale stellar bar which has a semi-major axis of  $28''$  (5.2 kpc). The circumnuclear CO ( $J=1 \rightarrow 0$ ) total intensity map (greyscale) is superposed, but note that its half power beam is only  $65''$  (6.1 kpc). (b) *I*-band image with the same field of view as the *K*-band image in (a). Two relatively straight dust lanes extend along the major axis of the large-scale stellar bar and are offset towards its leading edge. These dust lanes do not cross the center of the galaxy, but rather cross the bar minor axis and connect to a ring of star formation of radius  $\sim 4''$  (380 pc). (c) The CO ( $J=1 \rightarrow 0$ ) total intensity map (contours) is displayed on the same scale as (a) and (b) to facilitate comparisons. NGC 6951 has two spiral-shaped CO arms where the emission peaks at a radius  $r \sim 6''$  (570 pc). The two CO peaks lie almost along the minor axis of the bar and the CO arms connect to the two relatively straight dust lanes on the leading edge of the large-scale stellar bar. The CO and dust morphology are consistent with the piling up of gas near the OILR.

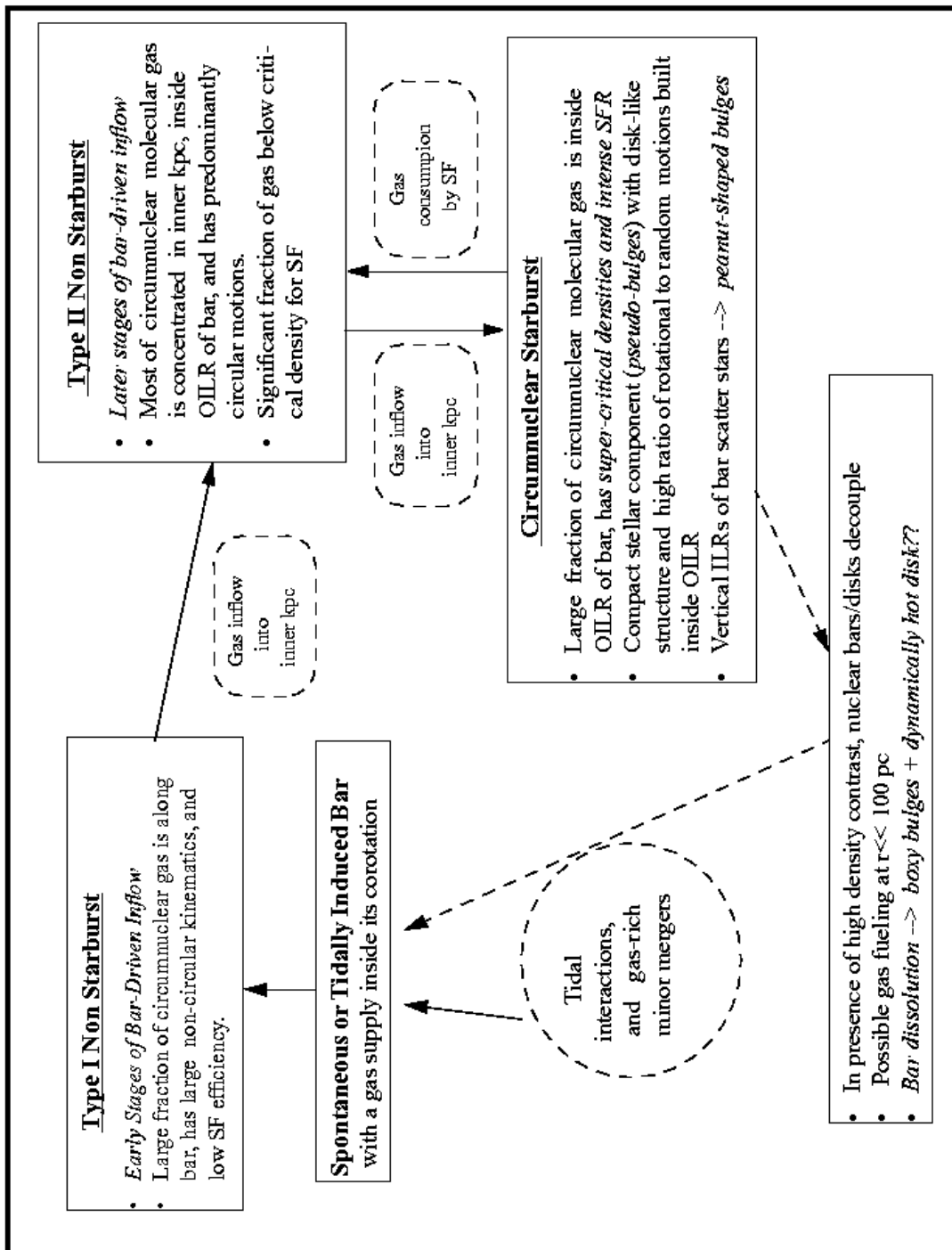


**Fig. 11— Bar-Driven Secular Evolution:** This figure sketches possible scenarios for bar-driven dynamical evolution and postulates potential evolutionary connections between the barred starbursts and non-starbursts in our sample. We suggest that a strongly barred galaxy would show up as a Type I non-starburst in the early stages of bar-driven inflow where large amounts of gas are still inflowing along the bar, have large non-circular motions, and are not forming stars efficiently. In the later stages where most of the circumnuclear gas has piled up inside the OILR of the bar, we may see a Type II non-starburst or even a circumnuclear starburst if most of the gas exceeds a critical density. The latter seems well represented by the Toomre value in our sample. Pseudo-bulges (Kormendy 1993) or compact stellar components with disk-like properties can be built in the inner kpc, as seen in our sample galaxy NGC 3351. Over its lifetime, a disk galaxy can undergo numerous episodes of bar-driven gas inflow and gradually build up its central mass concentration and bulge, provided an adequate gas supply is maintained inside the corotation radius of the bar. However, if the central mass concentration becomes large enough, bar dissolution may occur, leaving behind a dynamically hot disk. It is as yet unclear if tidal interactions and gas-rich accretions can lead to viable recurrent bar formation in such a disk.

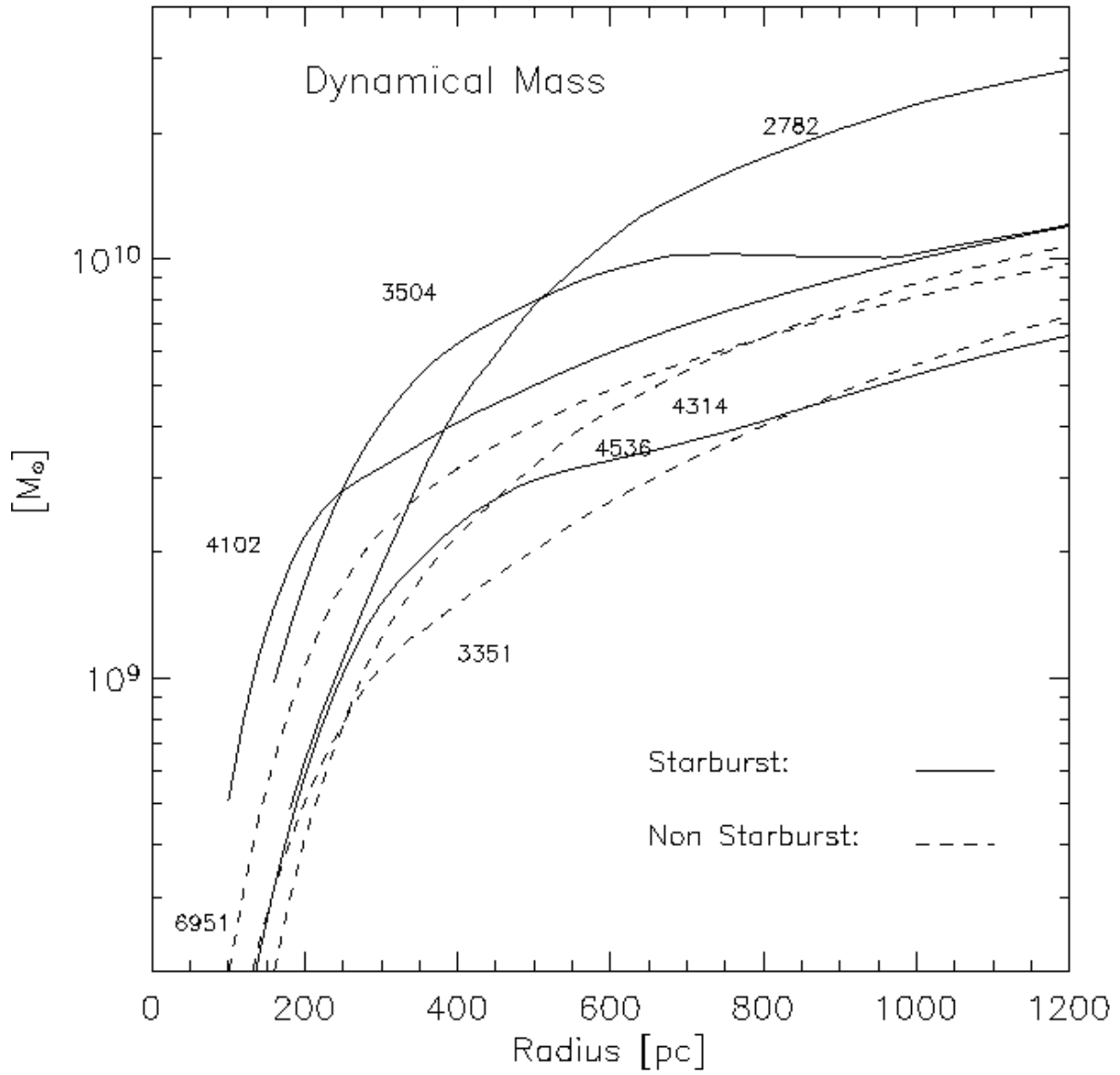


**Fig. 12— The enclosed dynamical mass within the inner kpc:** The dynamical mass ( $M_{dyn}$ ) enclosed within a given radius  $R$  is estimated from the rotation curve, assuming a spherically symmetric gas distribution. Values are shown only for sample barred galaxies where a reliable rotation curve can be derived. For  $R=1$  kpc,  $M_{dyn}$  has a range of  $6\text{--}30 \times 10^9 M_{\odot}$ .

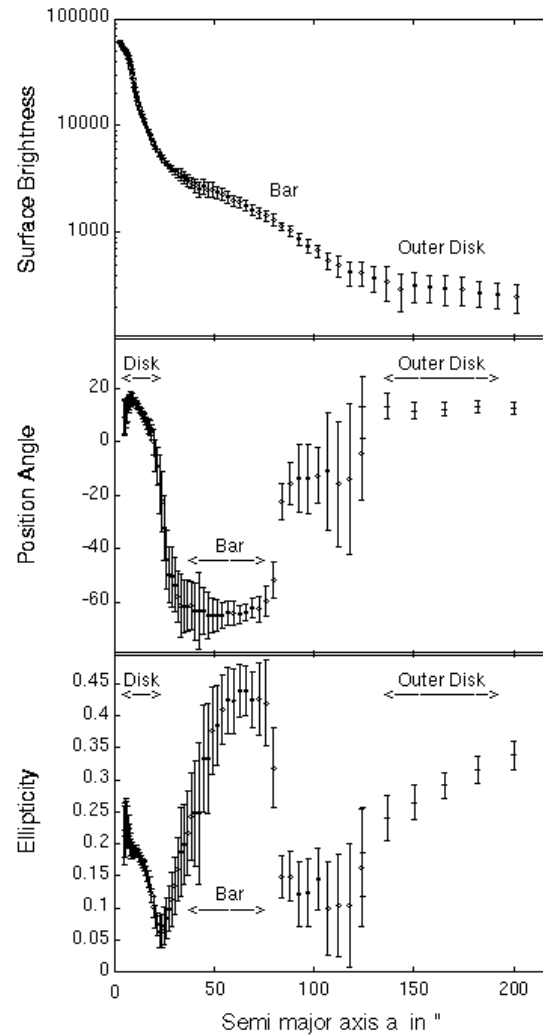


**Fig. 13— Evidence for a pseudo-bulge or compact disk in NGC 3351?** The isophotal analysis of the *K*-band and *R*-band images of NGC 3351 is shown. Inside the inner kpc radius, the ellipticity rises from a minimum value of 0.05 at  $r \sim 1$  kpc to a maximum of  $\sim 0.2$  at a radius of  $5''$  (250 pc). The position angle (P.A.) of the isophotes change from  $-60\text{deg}$  in the region of the large-scale stellar bar to a value between  $5$  and  $20\text{deg}$  in the central  $5''$  (250 pc) radius. The central component has an ellipticity and P.A. which is similar to that of the outer disk, and a published high ratio of rotational to random motions.

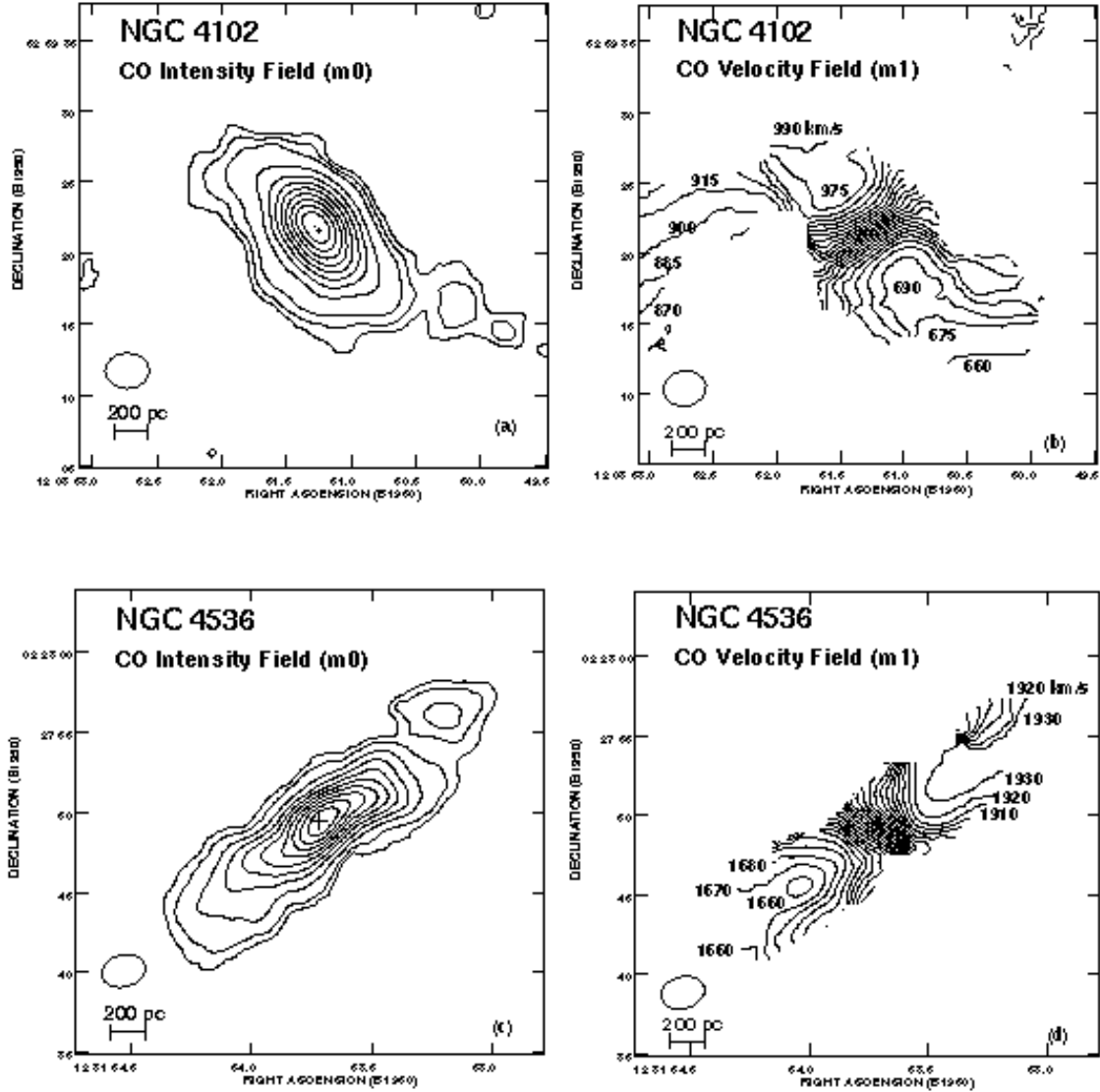


**Fig.14— Molecular gas kinematics and distribution in individual starbursts:** The CO intensity-weighted velocity (moment 1) fields and the CO total intensity (moment 0) maps of the starbursts NGC 4102 (a-b), NGC 4536 (c-d), NGC 3504 (e-f), NGC 470 (g-h), and NGC 2782 (i-j) are shown. The size of the synthesized beam is shown next to each map. The contour levels plotted are specified in Table 10. Relatively axisymmetric annuli or disks (NGC 4102, NGC 3504, NGC 4536) and elongated double-peaked morphologies (NGC 2782) are seen. The velocity field in the inner 500 pc radius is generally dominated by circular motions, with weaker non-circular components. In NGC 4102 and NGC 4536, there are faint gas streams which extend out, intersect the dust lanes on the leading edges of the large-scale stellar bar, and show non-circular motions. In NGC 2782, there are weak bar-like streaming motions in the inner 400 pc radius, on the leading side of a nuclear stellar bar.

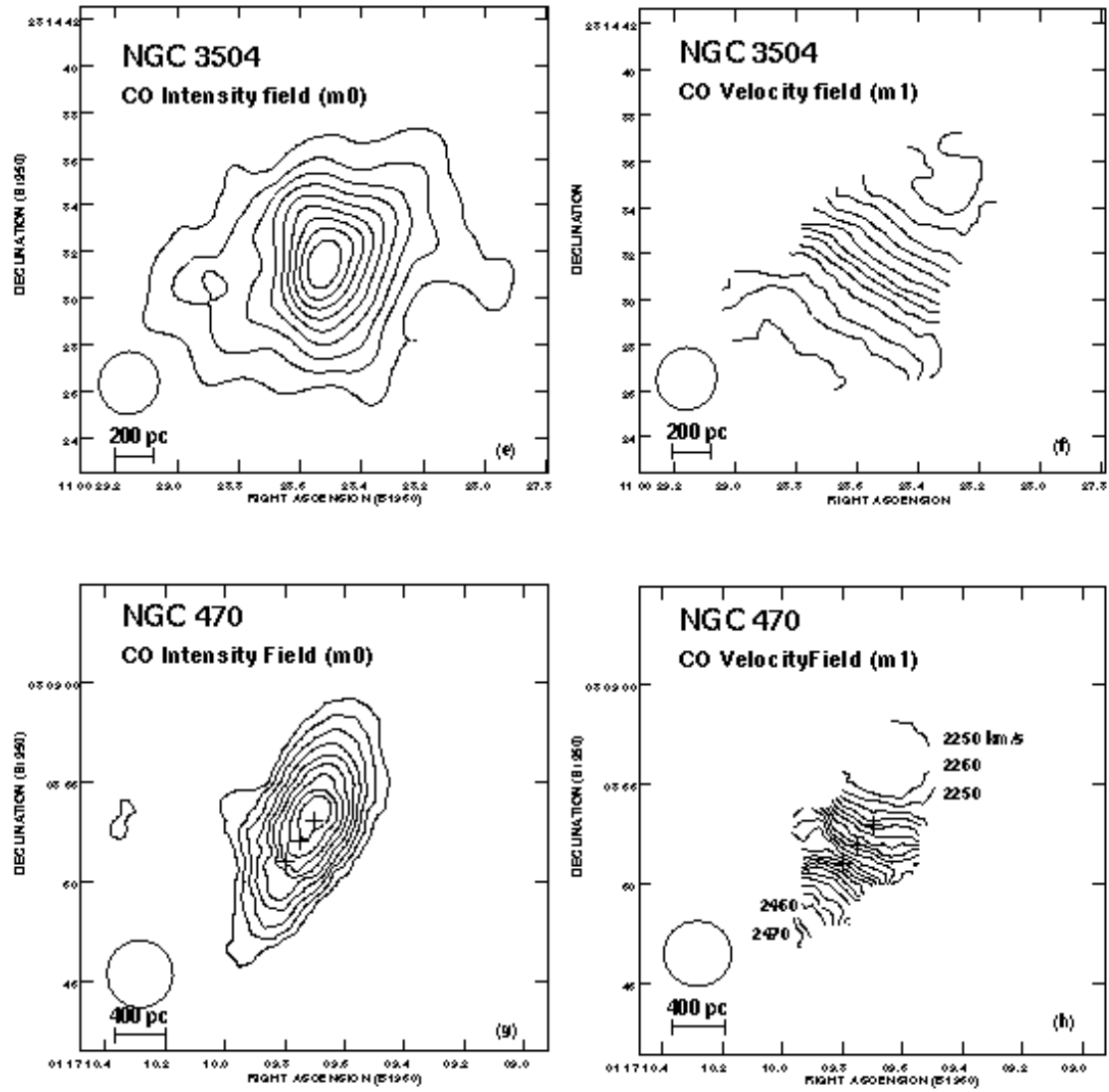


Fig.14— Continued

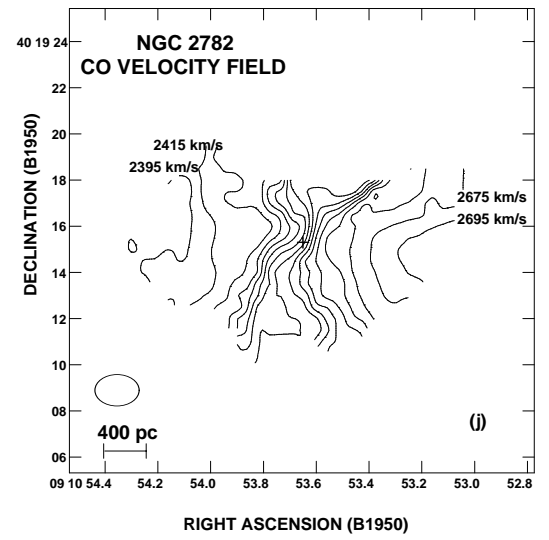
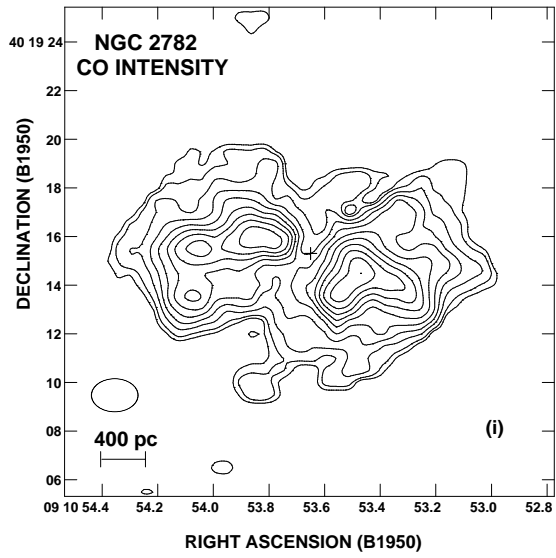
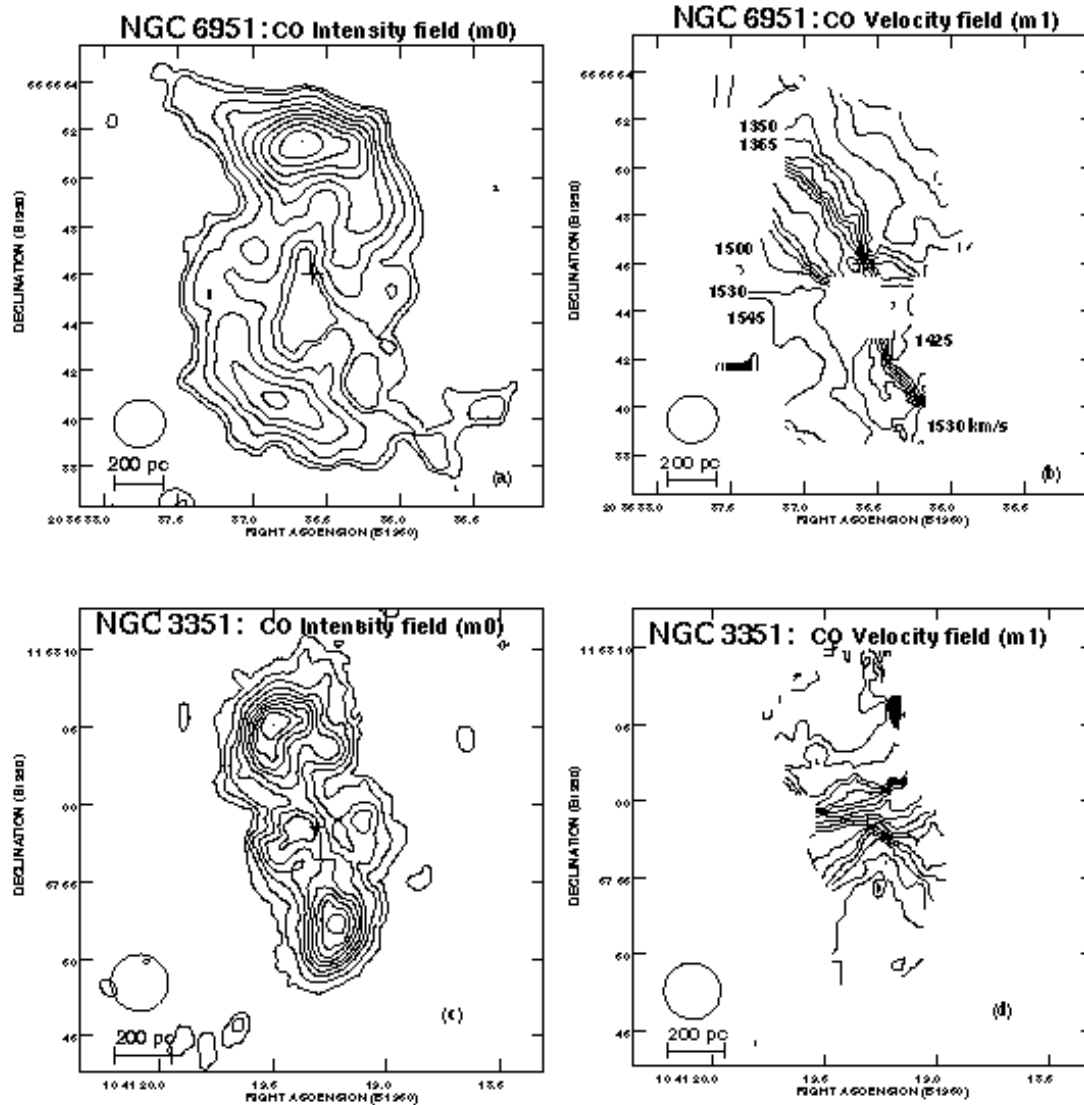


FIG. 14.— Continued



**Fig. 15— Molecular gas kinematics and distribution in the individual non-starbursts:** As in Fig. 14, but for non-starbursts NGC 6951 (a-b), NGC 3351 (c-d), and NGC 4314 (e-f). The contour levels plotted are specified in Table 10. NGC 6951 has two spiral-shaped CO arms where the CO emission peaks at a radius  $r \sim 6''$  (570 pc). NGC 3351 hosts two CO peaks at a radius  $r \sim 7''$  (350 pc). In NGC 4314, there is a relatively circular CO ring of  $8''$  (400 pc) radius from which extend two CO spurs/streams. The CO peaks in both NGC 6951 and NGC 3351 lie almost along the minor axis of the large-scale stellar bar. The CO arms in NGC 6951, the fainter emission around the CO peaks in NGC 3351, and the two CO spurs in NGC 4314 intersect the dust lanes on the leading edge of the large-scale stellar bar and show non-circular motions.

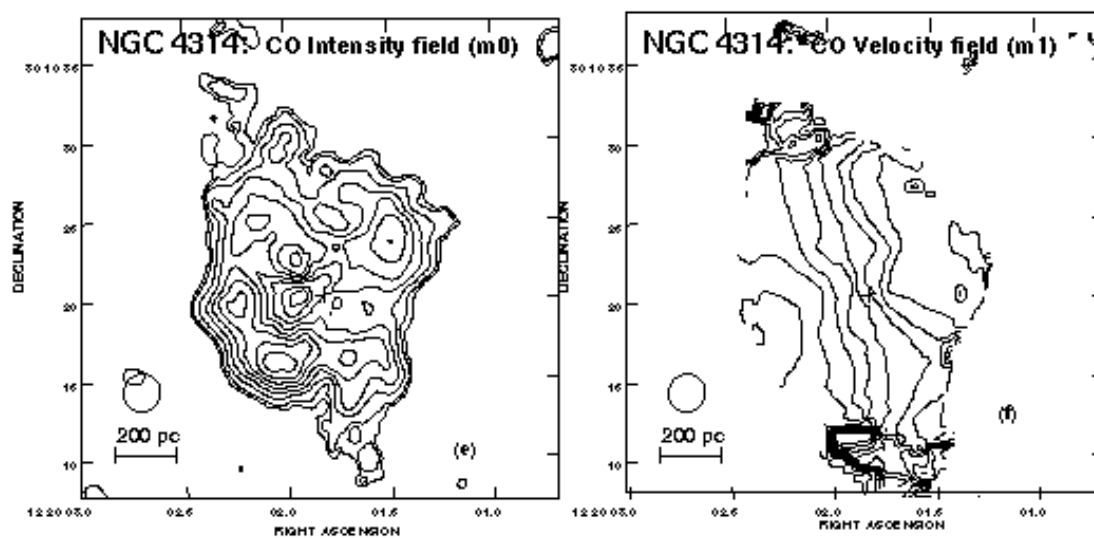


Fig.15— Continued

TABLE 1  
THE SAMPLE

NGC	R.A. (1950.0)	Dec (1950.0)	Type (RC3)	$i$ (deg)	$D$ (Mpc)	$D_{25}$ ( $'$ )	$m_B$	Notes
(1)	(2)	(3)	(4)	(5)	(6)	(7)	(8)	(9)
CIRCUMNUCLEAR STARBURSTS								
NGC 470	01:17:10.5	03:08:53	SABb(rs)	57	30.5	3.2	12.37	D,HII
NGC 2782 (Arp 215)	09:10:54.1	40:19:18	SABa(rs)pec	30	34	3.9	12.0	D,HII
NGC 3504	11:00:28.1	28:14:35	SABab(s)	22	20.0	2.6	11.74	D,HII
NGC 4102	12:03:51.6	52:59:23	SABb(s)	52	17.0	3.1	12.13	D,L
NGC 4536	12:31:53.6	02:27:50	SABbc(rs)	66	18.0	6.3	10.60	HII,L
CIRCUMNUCLEAR NON-STARBURSTS								
NGC 3351	10:41:19.7	11:58:00	SBb(r)	46	10.1	7.5	10.28	HII
NGC 3359	10:43:21.1	63:29:11	SBc(rs)	55	19.2	7.2	10.83	HII
NGC 4314	12:20:2.1	30:10:25	SBa(rs)	21	9.7	4.2	11.28	L
NGC 4569	12:34:18.7	13:26:20	SABab(rs)	64	16.8	8.8	9.86	HII,L
NGC 6951	20:36:37.7	65:55:48	SABbc(rs)	44	18.8	3.7	11.18	SEY2

Note. — Columns are : (1) NGC number; (2) (3) Right Ascension and Declination (Equinox 1950.0) of the optical center, from the Third Reference Catalog of Bright Galaxies, hereafter RC3 (de Vaucouleurs et al. 1991); (4) Hubble types from RC3; (5)  $i$  in degrees, the inclination of the galaxy. Sources are : NGC 2782 (Jogee et al. 1998, 1999), NGC 3351 (Grosbol 1985), NGC 3359 (Martin & Roy 1995), NGC 6951 (Grosbol 1985), NGC 4314 (Benedict et al. 1996), and the Nearby Galaxies (NBG) Catalogue (Tully 1988) for the remaining galaxies. (6)  $D$ , the adopted distance in Mpc. Sources are : NGC 4536 (Saha et al. 1996), NGC 3504 (Kenney et al. 1993), NGC 2782 (Jogee et al. 1998, 1999), and for the remaining galaxies, the NBG Catalogue (Tully 1988) which assumes a Hubble constant of  $75 \text{ km s}^{-1} \text{ Mpc}^{-1}$ ; (7)  $D_{25}$  in arcminutes, the diameter of the isophote where the surface brightness is 25 magnitude arcsecond $^{-2}$  in blue light. Values are from the NBG Catalogue (Tully 1988). (8)  $m_B$ , the blue apparent magnitude corrected for reddening, from the NBG Catalogue (Tully 1988); (9) Description of the nuclear activity and optical emission line spectrum of the galaxy. D denotes a galaxy belonging to Devereux's (1989) sample of circumnuclear starbursts. H denotes an HII region-like spectrum (Giuricin et al. 1994), L denotes a LINER (Giuricin et al. 1994), and SEY2 denotes a Seyfert 2 (Giuricin et al. 1994; Wozniak et al. 1995).

TABLE 2  
SINGLE DISH CO LUMINOSITIES AND TRACERS OF STAR FORMATION

NGC	$S_{\text{CO,S}}$ 45'' (Jy $\text{kms}^{-1}$ )	$L_{\text{CO}}$ 45'' ( $L_{\odot}$ )	$L_{\text{RC}}$ 45'' ( $L_{\odot}$ )	$L_{10\mu\text{m}}$ 5'' - 10'' ( $L_{\odot}$ )	$L_{\text{FIR}}$ Global ( $L_{\odot}$ )	$L_{\text{RC}}/L_{\text{CO}}$ 45'' (7)
(1)	(2)	(3)	(4)	(5)	(6)	(7)
CIRCUMNUCLEAR STARBURSTS						
470	68	3.83	4.17	9.12	10.21	2.10
2782	266	4.50	4.72	9.02	10.42	1.60
3504	450	4.30	4.60	9.11	10.31	1.99
4102	572	4.26	4.50	9.23	10.55	1.74
4536	607	4.33	4.35	8.77	10.32	1.03
CIRCUMNUCLEAR NON-STARBURSTS						
3351	479	3.73	3.28	7.51	9.52	0.35
3359	162	3.82	3.19	—	9.90	0.23
4314	251	3.41	2.62	<7.38	8.78	0.16
4569	870	4.43	3.62	8.48	9.98	0.15
6951	496	4.28	3.85	—	9.95	0.37

Note. — Columns are : (1) NGC number; (2)  $S_{\text{CO,S}}$  in  $\text{Jy km s}^{-1}$ , the single dish CO flux measured in the central 45'' for all galaxies, except NGC 4314 where the aperture is 55''.  $S_{\text{CO,S}}$  was estimated from observations with the Five College Radio Observatory (FCRAO) 14-m dish (Young et al. 1995) and NRAO 12-m single dish observations (Sage 1993). To derive flux densities  $S_{\text{CO,S}}$  in units of  $\text{Jy km s}^{-1}$  from the integrated intensity  $I_{\text{CO}}$  in units of  $\text{K}(T_A^*) \text{ km s}^{-1}$ , we adopted a main beam efficiency of  $42 \text{ Jy K}^{-1}$  and  $35 \text{ Jy K}^{-1}$  respectively for the FCRAO (Young et al. 1995), and NRAO (e.g., Maiolino et al. 1997) observations, and a source-beam coupling efficiency of 0.7; (3)  $L_{\text{CO}}$  in logarithmic units of  $L_{\odot}$ , the single dish CO luminosity determined from  $S_{\text{CO,S}}$ ; (4)  $L_{\text{RC}}$  in logarithmic units of  $L_{\odot}$ , the RC luminosity at 1.5 GHz in the central 45'' (Condon et al. 1990); (5)  $L_{10\mu\text{m}}$  in logarithmic units of  $L_{\odot}$ , the nuclear  $10 \mu\text{m}$  luminosity in a central 5''-10'' aperture (Giuricin et al. 1994); (6)  $L_{\text{FIR}}$  in logarithmic units of  $L_{\odot}$ , the far-infrared luminosity from the whole galaxy, measured in a bandpass  $80 \mu\text{m}$  wide centered on a wavelength of  $82.5 \mu\text{m}$ , from the IRAS Bright Galaxy Sample (Soifer et al. 1989); (7)  $L_{\text{RC}}/L_{\text{CO}}$ , the ratio of the RC luminosity at 1.49 GHz to the CO luminosity. Both luminosities are measured within the same 45'' aperture, except for NGC 4314.

TABLE 3  
EXTERNAL DISTURBANCES AND LARGE-SCALE STELLAR BARS

NGC (1)	Bar Type <sup>f</sup> (2)	Evidence for External Disturbances (3)
<b>CIRCUMNUCLEAR STARBURSTS</b>		
470	SAB	Outer disk has asymmetric H $\alpha$ emission <sup>h</sup> and shows evidence for warping. A recent interaction with 474 <sup>b</sup> is likely.
2782	SAB	Outer galaxy shows HI tails, optical tails, and ripples. <sup>c,d,e</sup> A close and intermediate mass-ratio interaction with a disk galaxy <sup>c</sup> is likely.
3504	SAB	Belongs to a group. <sup>k</sup> Possibly interacting with the small galaxy 3512.
4102	SAB	Belongs to a group whose brightest member is NGC 3992. <sup>j</sup>
4536	SAB	Is in the Southern Extension of the Virgo cluster. <sup>l</sup> Possibly interacting with 4527.
<b>CIRCUMNUCLEAR NON-STARBURSTS</b>		
3351	SB	Belongs to a group. <sup>k</sup>
3359	SB	Shows evidence <sup>m,n</sup> for a bar which is young and possibly tidally triggered. Has a possible small bound companion. <sup>g</sup>
4314	SB	Belongs to a group. <sup>11</sup> Outer disk is unusually gas poor. The total HI to H <sub>2</sub> mass ratio is unusually low ( $\sim 0.02$ )
4569	SAB	Is located in projection within 2 deg of the center of the Virgo Cluster. Has anemic spiral structures <sup>o</sup> and a truncated HI disk. <sup>i</sup> Optical images <sup>a</sup> suggest an outer warped disk. In the inner 3.5 kpc radius, the K-band image <sup>h</sup> shows an asymmetric bar, and the molecular gas has very disturbed kinematics <sup>h</sup> .
6951	SAB	Isolated galaxy.

Note. — Columns are : (1) NGC number; (2) Bar Type according to RC3 (de Vaucouleurs et al. 1991); (3) Evidence for External Disturbances

References. — a. Sandage & Bedke 1994; b. Schweizer & Seitzer 1988; c. Smith 1994; d. Jogee et al. 1998 ; e. Jogee et al. 1999; f. RC3 (de Vaucouleurs et al. 1991); g. Ball 1986; h. Jogee 1999 ; i. Giovanelli & Haynes 1983; j. Geller & Huchra 1983 ; k. Tully 1988; l. Bingelli, Sandage, & Tammann 1985; m. Friedli, Benz, & Kennicutt 1994; n. Martin & Roy 1995; o. van den Bergh 1976;

TABLE 4  
CO (J=1-> 0) OBSERVATIONS & CHANNEL MAPS

NGC (1)	Synthesised Beam (2)	Weight (3)	R.m.s. noise (mJy/Beam) (4)	T <sub>B</sub> for 1 Jy/Beam (K) (5)
470	3.61" x 3.46" = 550x530 pc	U	22.0	7.4
2782	2.14" x 1.52" = 364x258 pc	U	13.0	28.2
	2.62" x 1.98" = 445x337 pc	N	10.5	17.7
3504	2.50" x 2.40" = 250x240 pc	U	35.0	15.3
4102	2.40" x 1.96" = 204x167 pc	U	15.0	19.5
	3.12" x 2.56" = 265x218 pc	N	13.0	11.5
4536	2.63" x 1.88" = 235x170 pc	U	15.0	18.6
	2.82" x 2.37" = 255x215 pc	N	12.0	13.7
3351	2.38" x 2.34" = 120x118 pc	U	30.0	16.5
3359	3.38" x 2.91" = 324x279 pc	N	16.0	9.3
4314	2.29" x 2.17" = 110x105 pc	U	28.0	18.5
	3.12" x 2.70" = 150x130 pc	N	22.0	10.9
4569	2.65" x 2.01" = 225x170 pc	U	16.0	9.7
	3.22" x 2.95" = 275x251 pc	N	14.0	17.4
6951	2.28" x 2.11" = 110x102 pc	U	19.2	19.1

Note. — Columns are : (1) NGC number; (2) The size of the synthesized beam ; (3) The weighting used for the channel maps: 'U' refers to uniform and 'N' to natural weighting; (4) The r.m.s. noise in mJy beam<sup>-1</sup> for the channel maps; (5) The equivalent brightness temperature (T<sub>B</sub>) in K for 1 Jy beam<sup>-1</sup>.

TABLE 5  
CIRCUMNUCLEAR MOLECULAR PROPERTIES

NGC	$S_{\text{CO,I}}$	$M_{\text{H}_2}$	$V_{\text{sys}}$	$f_{\text{SD}}$
(1)	(Jy km s <sup>-1</sup> ) (2)	( $M_{\odot}$ ) (3)	(km s <sup>-1</sup> ) (4)	(%) (5)
CIRCUMNUCLEAR STARBURST				
470	53	5.0E8	2350	80
2782	184	2.3E9	2555	65
3504	280	1.2E9	1535	71
4102	450	1.4E9	835	80
4536	355	1.2E9	1800	60
CIRCUMNUCLEAR NON-STARBURSTS				
3351	241	2.7E8	780	60
3359	20	8.0E7	-	12 <sup>1</sup>
4314	248	2.6E8	983	92
4569	550	1.7E9	-235	65
6951	299	1.2E9	1431	60

Note. — Columns are : (1) NGC number; (2)  $S_{\text{CO,I}}$  in Jy km s<sup>-1</sup>, the flux detected by the OVRO interferometric observations; (3)  $M_{\text{H}_2}$  in solar units, the mass of molecular hydrogen corresponding to  $S_{\text{CO,I}}$ , if one assumes a standard Galactic CO-to-H<sub>2</sub> conversion factor; (4)  $V_{\text{sys}}$  in km s<sup>-1</sup>, the systemic velocity estimated from the moment 1 map. (5)  $f_{\text{SD}}$ , the fraction of the single dish flux detected by the interferometric observations. See text for a discussion of the low  $f_{\text{SD}}$  for NGC 3359.

TABLE 6  
MOLECULAR ENVIRONMENTS IN THE CIRCUMNUCLEAR REGION VS. THE OUTER DISK

Quantities <sup>a</sup>	Outer Disk of Normal Sa-Sc Spirals	Inner 500 pc radius of Sample Starbursts and Non Starbursts	Inner 500 pc radius of ULIRG Arp 220
(1) $M_{\text{gas,m}}$ [ $M_{\odot}$ ]	$\leq \text{few} \times 10^9$ <sup>b</sup>	Few $\times (10^8\text{-}10^9)$ <sup>c</sup>	$3 \times 10^9$ <sup>d</sup>
(2) $M_{\text{gas}}/M_{\text{dyn}}$ [%]	$< 5$ <sup>e</sup>	10 to 30 <sup>c</sup>	40 to 80 <sup>d</sup>
(3) SFR [ $M_{\odot} \text{ yr}^{-1}$ ]	-	0.1-11 <sup>c</sup>	$> 100$ <sup>g</sup>
(4) $\Sigma_{\text{gas,m}}$ [ $M_{\odot} \text{ pc}^{-2}$ ]	1-100 <sup>f</sup>	500 to 3500 <sup>c</sup>	$4 \times 10^4$ <sup>d</sup>
(5) $\sigma$ [km s <sup>-1</sup> ]	6-10 <sup>h</sup>	10 to 40 <sup>i</sup>	90 <sup>g</sup>
(6) $\kappa$ [km s <sup>-1</sup> kpc <sup>-1</sup> ]	$< 100$ <sup>j</sup>	800 to 3000 <sup>c</sup>	$> 1000$ <sup>g</sup>
(7) $\Sigma_{\text{crit}}$ [ $M_{\odot} \text{ pc}^{-2}$ ]	$< 10$ <sup>k</sup>	500-1500 <sup>l</sup>	2200 <sup>m</sup>
(8) $t_{\text{GI}}$ [Myr]	$> 10$ <sup>k</sup>	0.5-1.5 <sup>l</sup>	0.5 <sup>m</sup>
(9) $\lambda_{\text{J}}$ [pc]	Few $\times (100\text{-}1000)$ <sup>k</sup>	100-300 <sup>l</sup>	90 <sup>m</sup>
(10) $M_{\text{J}}$ [ $M_{\odot}$ ]	Few $\times (10^7\text{-}10^6)$ <sup>k</sup>	Few $\times (10^7\text{-}10^8)$ <sup>l</sup>	$8 \times 10^8$ <sup>m</sup>

Note. — Rows are : (1)  $M_{\text{gas,m}}$  in  $M_{\odot}$ , the molecular gas content including hydrogen and helium. A standard CO-to-H<sub>2</sub> conversion factor and a solar metallicity are assumed; (2)  $M_{\text{gas,m}}/M_{\text{dyn}}$  in %, the ratio of molecular gas mass to dynamical mass; (3)  $\Sigma_{\text{gas,m}}$  in  $M_{\odot} \text{ pc}^{-2}$ , the molecular gas surface density; (4)  $\Sigma_{\text{SFR}}$  in  $M_{\odot} \text{ yr}^{-1} \text{ pc}^{-2}$ , the SFR per unit area; (5)  $\sigma$  in km s<sup>-1</sup>, the gas velocity dispersion; (6)  $\kappa$  in km s<sup>-1</sup> kpc<sup>-1</sup>, the epicyclic frequency; (7)  $\Sigma_{\text{crit}}$  in  $M_{\odot} \text{ pc}^{-2}$ , the critical density for the onset of gravitational instabilities as defined in § 5.3.1, with  $\alpha = 0.7$ ; (8)  $t_{\text{GI}} = Q/\kappa$  in Myr, the growth timescale of the most unstable wavelength associated with gravitational instabilities, assuming  $Q \sim 1$ ; (9)  $\lambda_{\text{J}}$  in pc, the Jeans length (10)  $M_{\text{J}}$  in  $M_{\odot}$ , the Jeans mass.

Note. — <sup>a</sup> Typical values are quoted for the quantities. Individual cases may vary; <sup>b</sup> Young & Scoville 1991; <sup>c</sup> This work; <sup>d</sup> Sakamoto et al. (1999), for a self-gravitating gas disk. Quoted mass is the sum for Arp 220 W and E; <sup>e</sup> Binney & Tremaine 1987; <sup>f</sup> Devarheng et al. 1994; <sup>g</sup> Scoville, Yun, and Bryant 1997 <sup>h</sup> Dickey et al. 1990; <sup>i</sup> The upper limit for the velocity dispersion is quoted after correcting for beam smearing; <sup>j</sup> Larson 1988; <sup>k</sup> For the outer disk, (7) to (10) are computed for  $\kappa < 100 \text{ km s}^{-1} \text{ kpc}^{-1}$ ,  $\sigma \sim 6 \text{ km s}^{-1}$ , and  $\Sigma_{\text{gas,m}} = 10\text{-}100 M_{\odot} \text{ pc}^{-2}$ ; <sup>l</sup> Quantities (7) to (10) are computed at  $r=250 \text{ pc}$  in the circumnuclear starbursts and non-starbursts NGC 4102, NGC 4536, NGC 3504, NGC 3351 and NGC 4314; <sup>m</sup> Quantities (7) to (10) are computed for Arp 220 W assuming  $\kappa \sim 2000 \text{ km s}^{-1} \text{ kpc}^{-1}$ ,  $\sigma \sim 90 \text{ km s}^{-1}$ , and  $\Sigma_{\text{gas,m}} \sim 4 \times 10^4 M_{\odot} \text{ pc}^{-2}$ .

TABLE 7  
SF RATES FROM FIR, RC, AND BR $\gamma$  DATA

NGC	Based on global $L_{\text{FIR}}$ $L_{\text{FIR}}, \text{SFR}_{\text{FIR}}$ ( $L_{\odot}, M_{\odot} \text{ yr}^{-1}$ )	Based on RC $\nu, S_{\nu}, R_{\text{RC}}, \text{SFR}_{\text{RC-N}}$ (GHz, mJy, pc, $M_{\odot} \text{ yr}^{-1}$ )	Based on Br $\gamma$ $R_{\text{Br}\gamma}, N_{\text{Ly}}, \text{SFR}_{\text{Br}\gamma}$ (pc, $\text{s}^{-1}, M_{\odot} \text{ yr}^{-1}$ )
(1)	(2)	(3)	(4)
CIRCUMNUCLEAR STARBURSTS			
470	10.21, 6.3	1.5, 26.6 <sup>a</sup> , 1680, 2.8	-
2782	10.42, 10.2	1.5, 107 <sup>a</sup> , 2210, 13.8 4.9, 40 <sup>e</sup> , 1700, 11.6	1650, 5.0E53 <sup>g</sup> , 5.6
3504	10.31, 8.0	1.5, 230 <sup>a</sup> , 800, 10.2	945, 1.5E53 <sup>g</sup> , 2.8
4102	10.55, 13.8	1.5, 227 <sup>a</sup> , 1105, 7.3	945, 9.2E52 <sup>g</sup> , 1.1
4536	10.32, 8.1	1.5, 149 <sup>a</sup> , 1800, 5.4 4.9, 61 <sup>f</sup> , 900, 4.9	840, 4.0E53 <sup>g</sup> , 4.8
CIRCUMNUCLEAR NON-STARBURSTS			
3351	9.52, 1.3	1.5, 28 <sup>b</sup> , 1000, 0.3	490, 6.0E52 <sup>g</sup> , 0.5
3359	9.90, 3.1	1.5, 50 <sup>a</sup> , 20160, 2.1	-
4314	8.78, 0.2	1.5, 12.5 <sup>c</sup> , 3640, 0.1	-
4569	9.98, 3.7	1.5, 83 <sup>c</sup> , 8420, 2.5	-
6951	9.95, 3.5	4.9, 14 <sup>e</sup> , 750, 1.2	-

Note. — Columns are : (1) NGC number; (2)  $L_{\text{FIR}}$  in logarithmic units of  $L_{\odot}$ , the global FIR luminosity;  $\text{SFR}_{\text{FIR}}$  in  $M_{\odot} \text{ yr}^{-1}$ , the global SFR for the entire galaxy; (3)  $\nu$  in GHz, the frequency of the RC observations;  $S_{\nu}$  in mJy, the RC flux density;  $R_{\text{RC-N}}$  in pc, the radius within which more than 90 % of the RC emission is concentrated;  $\text{SFR}_{\text{RC-N}}$  in  $M_{\odot} \text{ yr}^{-1}$ , the SFR within  $R_{\text{RC}}$ , estimated from the non-thermal component of the radio continuum flux density; (4)  $R_{\text{Br}\gamma}$  in pc, the aperture radius for the Br $\gamma$  observations;  $N_{\text{Ly}}$  in  $\text{s}^{-1}$ , the number of Lyman continuum photons per seconds from Puxley et al. (1990);  $\text{SFR}_{\text{Br}\gamma}$  in  $M_{\odot} \text{ yr}^{-1}$ , the SFR within  $R_{\text{Br}\gamma}$ .

References. — a. Condon et al. 1990; b. Condon, Anderson, & Broderick 1995; c. Condon 1987; d. Hummel et al. 1985; e. Saikia et al. 1994; f. Villa et al. 1990; g. Puxley et al. 1990

TABLE 8  
ADOPTED CIRCUMNUCLEAR SFRs OVER RADIUS OF CO EMISSION

NGC	$R_{\text{CO}}$ (pc)	$M_{\text{H}_2}$ ( $M_{\odot}$ )	$\text{SFR}_{\text{CO}}$ ( $M_{\odot} \text{ yr}^{-1}$ )	$\text{SFR}_{\text{CO}}/M_{\text{H}_2}$ ( $\text{yr}^{-1}$ )	$t_{\text{SFR}}$ ( $10^8 \text{ yrs}$ )
(1)	(2)	(3)	(4)	(5)	(6)
CIRCUMNUCLEAR STARBURST					
470	1100	5.0E8	3	6E-9	2
2782	1530	1.8E9	11	6E-9	2
3504	1300	1.2E9	10	8E-9	1
4102	1275	1.4E9	7	5E-9	2
4536	1300	1.2E9	5	4E-9	2
CIRCUMNUCLEAR NON-STARBURSTS					
3351	600	5.3E8	0.5	9E-10	11
4314	590	2.3E8	<0.1	< 4E-10	> 25
4569	1680	1.6E9	<1.2	> 7E-10	> 14

Note. — Columns are : (1) NGC number; (2)  $R_{\text{CO}}$  in pc, the radius of CO emission; (3)  $M_{\text{H}_2}$  in  $M_{\odot}$ , the mass of molecular hydrogen within a radius  $R_{\text{CO}}$ ; (4)  $\text{SFR}_{\text{CO}}$  in  $M_{\odot} \text{ yr}^{-1}$ , the SF rate within  $R_{\text{CO}}$ ; (5) ( $\text{SFR}_{\text{CO}}/M_{\text{H}_2}$ ) in  $\text{yr}^{-1}$ , the SFR per unit mass of molecular hydrogen; (6)  $t_{\text{SFR}}$  in  $10^8$  years, the average gas consumption timescale by SF given by ( $M_{\text{H}_2}/\text{SFR}_1$ )

TABLE 9  
PRIMARY BAR PROPERTIES AND DYNAMICAL RESONANCES

NGC	Bar	$\epsilon_1$	PA <sub>1</sub>	a <sub>1</sub>	$M_{\text{gas,m}}$	$\frac{M_{\text{gas,m}}}{M_{\text{dyn}}}$	$\Omega_p$	$R_{OILR}$	$R_{IILR}$
(1)	(2)	(3)	(4)	(5)	(6)	(7)	(8)	(9)	(10)
470	AB	0.55 <sup>a</sup>	14 <sup>a</sup>	4.8 <sup>a</sup>	2E8	30	...	...	...
3504	AB	0.58 <sup>b</sup>	135 <sup>b</sup>	3.0 <sup>c</sup>	8E8	20	< 76	> 900	< 200
4102	AB	0.45 <sup>e</sup>	62 <sup>e</sup>	1.8 <sup>e</sup>	8E8	25	< 115	> 500	< 250
4536	AB	0.40 <sup>b</sup>	140 <sup>b,c</sup>	3.1 <sup>c</sup>	1E9	30	< 50	> 800	< 200
3351	B	0.57 <sup>d</sup>	115 <sup>c</sup>	2.2 <sup>c,d</sup>	2E8	17	< 85	> 300	< 300
3359	B	0.68 <sup>d</sup>	24 <sup>c</sup>	2.9 <sup>d</sup>	...	...	...	...	...
4314	B	0.69 <sup>a</sup>	143 <sup>a</sup>	3.6 <sup>a</sup>	2E8	9	< 78	> 700	< 200
4569	AB	...	15 <sup>e</sup>	...	2E8	...	...	...	...
6951	AB	0.59 <sup>a</sup>	85 <sup>a</sup>	5.2 <sup>a</sup>	3E8	21	< 43	> 650	< 300

Note. — Columns are : (1) NGC number; (2) Bar type from RC3 (de Vaucouleurs et al. 1991): B denotes a strong bar, and AB a bar of intermediate strength; (3) (4) (5)  $\epsilon_1$ , PA<sub>1</sub> in deg, a<sub>1</sub> in kpc, the ellipticity, position angle, and semi-major axis of the large-scale stellar bar; (6)  $M_{\text{gas,m}}$  [r=300] in  $M_{\odot}$ , the molecular gas mass enclosed within a 300 pc radius. A standard CO-to-H<sub>2</sub> conversion factor and a solar metallicity are assumed; (7)  $\frac{M_{\text{gas,m}}}{M_{\text{dyn}}}$  [r=300], the ratio of molecular gas mass to dynamical mass within a 300 pc radius; (8) Upper limit on  $\Omega_p$  in km s<sup>-1</sup> kpc<sup>-1</sup>, the primary bar pattern speed; (9) Upper limit on  $R_{OILR}$  in pc, the radius of the Outer Inner Lindblad Resonance; (10) Lower limit on  $R_{IILR}$  in pc, the radius of the Inner Inner Lindblad Resonance.

References. — a. Friedli et al. 1996; b. Pompea & Rieke 1990; c. Shaw et al. 1995; d. Martin 1995; e. This work.

TABLE 10  
CONTOUR LEVELS PLOTTED IN FIGURES

NGC	Figure	Contour levels
<b>CIRCUMNUCLEAR STARBURSTS</b>		
470	Figs. 3, 5, 14	Levels = 2.48 Jy beam <sup>-1</sup> km s <sup>-1</sup> × (1, 2, 3, 4, 5, 6, 7, 8, 9, 10)
470	Fig. 14	Levels = (2200, 2210, 2220, ....., 2470, 2480, 2490) km s <sup>-1</sup>
2782	Figs. 3, 5, 14	Levels = 7.15 Jy beam <sup>-1</sup> km s <sup>-1</sup> × (1, 2, 3, 4, 5, 6, 7, 8, 9, 10)
2782	Fig. 14	Levels = (2275, 2295, 2315, ....., 2815, 2835, 2855) km s <sup>-1</sup>
3504x	Figs. 3, 5, 14	Levels = 8.33 Jy beam <sup>-1</sup> km s <sup>-1</sup> × (0.5, 1, 2, 3, 4, 5, 6, 7, 8, 9, 10)
3504 x	Fig. 14	Levels = (585, 600, 615, ....., 990, 1005, 1020) km s <sup>-1</sup>
4102	Figs. 3, 5, 14	Levels = 8.33 Jy beam <sup>-1</sup> km s <sup>-1</sup> × (0.5, 1, 2, 3, 4, 5, 6, 7, 8, 9, 10)
4102	Fig. 14	Levels = (585, 600, 615, ....., 990, 1005, 1020) km s <sup>-1</sup>
4536	Figs. 3, 5, 14	Levels = 3.05 Jy beam <sup>-1</sup> km s <sup>-1</sup> × (1, 2, 3, 4, 5, 6, 7, 8, 9, 10)
4536	Fig. 14	Levels = (1640, 1650, 1660, ....., 1910, 1920, 1930) km s <sup>-1</sup>
<b>CIRCUMNUCLEAR NON-STARBURSTS</b>		
3351	Figs. 3, 5, 15	Levels = 1.84 Jy beam <sup>-1</sup> km s <sup>-1</sup> × (1, 2, 3, 4, 5, 6, 7, 8, 9, 10)
3351	Fig. 15	Levels = (660, 670, 680, ....., 930, 940, 950) km s <sup>-1</sup>
4314	Figs. 3, 5, 15	Levels = 1.34 Jy beam <sup>-1</sup> km s <sup>-1</sup> × (1, 2, 3, 4, 5, 6, 7, 8, 9, 10)
4314	Fig. 15	Levels = (915, 930, 945, ....., 1050, 1065, 1080) km s <sup>-1</sup>
4569	Figs. 3, 5, 15	Levels = 3.20 Jy beam <sup>-1</sup> km s <sup>-1</sup> × (1, 2, 3, 4, 5, 6, 7, 8, 9, 10)
6951	Figs. 3, 5, 15	Levels = 2.92 Jy beam <sup>-1</sup> km s <sup>-1</sup> × (1, 2, 3, 4, 5, 6, 7, 8, 9, 10)
6951	Fig. 15	Levels = (1275, 1290, 1305, ....., 1680, 1695, 1710) km s <sup>-1</sup>

Note. — Columns are : (1) NGC number; (2) Figures ; (3) Countour levels plotted.